JOURNAL OF AEROSPACE SOCIETY MALAYSIA

Volume 3

DECEMBER 2025

PERSATUAN AEROANGKASA MALAYSIA

Registration No. PPM-001-10-09012017

Toward Greater Heights

JOURNAL OF
AEROSPACE SOCIETY MALAYSIA

VOLUME 3
December 2025

eISSN 3009-0520
9 773009 052004

© 2025 published by Aerospace Society Malaysia

B-31-09, Kompleks EVO, Jalan Pusat Bandar 2, Seksyen 9,
43650 Bandar Baru Bangi, Selangor, Malaysia

Email: aeros_journal@aerosmalaysia.my

Journal of Aerospace Society Malaysia (AEROS Journal) is an open-access online journal that publishes high-quality research articles in all areas of aeronautics, astronautics and aviation. All submitted articles will undergo peer-review process before they are accepted for publication.

Publication Frequency: 1 time a year (end of December)

This journal is licensed under the Creative Commons Attribution-Non Commercial 4.0 International License.

EDITORIAL

EDITOR-IN-CHIEF

Assoc. Prof. Dr. Fairuz Izzuddin Romli

LIST OF REVIEWERS FOR THIS ISSUE

Assoc. Prof. Dr. Azmin Shakrine Mohd Rafie
Assoc. Prof. Dr. Nurul Zuhairah Mahmud Zuhudi
Dr. Ahmad Faiz Mohammad
Dr. Mohamad Amiruddin Ismail
Dr. Mohd Faisal Abdul Hamid
Dr. Mohd Na'im Abdullah
Dr. Nurul Zubaidah Zaki
Dr. Sarmad Dawood
Dr. Zurriati Mohd Ali

TABLE OF CONTENTS

JOURNAL OF
AEROSPACE SOCIETY MALAYSIA

ARTICLE

EXPERIMENTAL WIND TUNNEL TESTING OF SHARP-EDGED DELTA WING UNDER ROLLING AND PITCHING MOTION

Naderaj Vellan [1,*], Sakib Islam Fahim [1], Syazana Emran [1] and Shabudin Mat [2]

1. Faculty of Mechanical Engineering, Universiti Teknologi Malaysia, Malaysia.
2. UTM Aerolab, Institute for Sustainable Transport, Universiti Teknologi Malaysia, Malaysia.

*Correspondence: v.nadarraj@gmail.com

Abstract: This study presents an experimental investigation of aerodynamic characteristics of a sharp-edged delta wing that is undergoing controlled rolling and pitching motions in a low-speed wind tunnel. Delta wings have been distinguished by their distinctive capacity to maintain lift at high angles of attack as a result of formation of leading-edge vortices. The wind tunnel tests were conducted in the Universiti Teknologi Malaysia's Low-Speed Tunnel with a freestream velocity of 25 m/s, which corresponds to a Reynolds number of 1.288×10^6 based on the wing model's root chord. In the experiments, the delta wing model, designed with a 65° sweep angle, was subjected to sinusoidal rolling and pitching motions at amplitudes of 10° and frequencies of 1000 Hz. The surface pressure distributions were obtained by using an array of 106 pressure taps and they were corrected for solid blockage using the Maskell method. On the whole, the results reveal that unsteady motions significantly influence the vortex development, symmetry and breakdown location, with phase lags observed between the motion and the aerodynamic response. These findings provide an essential benchmark data for computational fluid dynamics (CFD) validation and aerodynamic design of maneuvering delta-wing configurations.

Keywords: delta wing, pitching motion, rolling motion, unsteady aerodynamics, vortex dynamics, wind tunnel testing

1. Introduction

Delta wings are a critical aerodynamic configuration in modern aerospace design as they are prized for their capability to maintain lift at high angles of attack through the formation of strong leading-edge vortices (LEVs). By postponing stall and enhancing maneuverability, the vortices further contribute to an enhanced aerodynamic performance of the aircraft. This vortex-dominated flow regime enables the superior maneuverability and high-lift performance, making delta wings the preferred choice for high-speed aircraft, unmanned aerial vehicles and agile platforms [1].

In steady conditions, the aerodynamics of delta wings can be taken to be already well understood, with classical works such as Gursul et al. that provides the foundation for vortex behavior in the non-slender configurations [2]. Moreover, several recent studies have expanded this understanding using high-fidelity experimental and numerical techniques. For instance, Zamzuddin et al. showed that sharp-edged delta wings exhibit notable changes in vortex stability when subjected to flow control via blowing [3]. However, it has been noted that the LEVs are highly sensitive to unsteady motions such as rolling and pitching, which can significantly alter the lift, drag and stability characteristics of the aircraft. These vortices are subject to intricate interactions that can result in vortex breakdown, abrupt lift fluctuations and differences in aerodynamic stability when subjected to dynamic conditions. It is therefore essential to comprehend the aerodynamic behaviors in order to enhance the design and control of contemporary high-performance aircraft.

Under the rolling motion, the unsteady effects can cause vortex asymmetry between advancing and retreating wing sides, leading to differences in the vortex core strength and also the breakdown onset. Roll rate and amplitude directly influence the breakdown location, with high roll rates producing earlier breakdown on the retreating side. Studies such as those by Lowson and Riley [4], and Gursul and Ho [5] have indicated several factors that could affect the variation of vortex breakdown position over the delta wing, including the wing's model geometry. Numerical simulations further revealed the coupled influence of roll oscillations and vortex stability, highlighting the complex phase-lag phenomena [6]. In the meantime, under the pitching motion, the unsteady aerodynamics are characterized by a phase lag between instantaneous angle of attack and aerodynamic response, which could shift vortex breakdown location and alter LEV coherence. Kumar et al. [7] experimentally investigated vortex topology changes during dynamic maneuvers of flying wings, revealing the significant deformation of vortex cores during pitch cycles. These findings align with some of the earlier observations on delta wings, confirming that unsteady pitching introduces dynamic effects that are absent in steady-state conditions [8].

Despite the advances, the comparative experimental datasets that capture both rolling and pitching effects on sharp-edged delta wings remain scarce. Such datasets are essential for the validation of the computational fluid dynamics (CFD) tools, particularly for maneuvering flight conditions. This present work addresses this gap through wind tunnel testing of a sharp-edged 65° delta wing model subjected to controlled rolling and pitching motions. The focus of the study is on the surface pressure distribution, vortex development and also breakdown behavior.

2. Methodology

The experimental investigation was conducted using a sharp-edged delta wing model with a chord length of 0.814 m and a sweep angle of 65°. The wing model was fabricated from lightweight aluminum to ensure rigidity during testing. Furthermore, a customized test rig was designed to mount the wing model inside the subsonic open-circuit wind tunnel. The rig allowed for precise adjustments of angle of attack, α and rolling motion, Φ, enabling a wide range of aerodynamic configurations to be tested. The wind tunnel has a test section with dimension of 1.2 m × 1.2 m and can be operated at a maximum velocity of 50 m/s. Figure 1 depicts the delta wing model used in this study while the test rig designed for the wind tunnel testing in this study is shown in Figure 2.

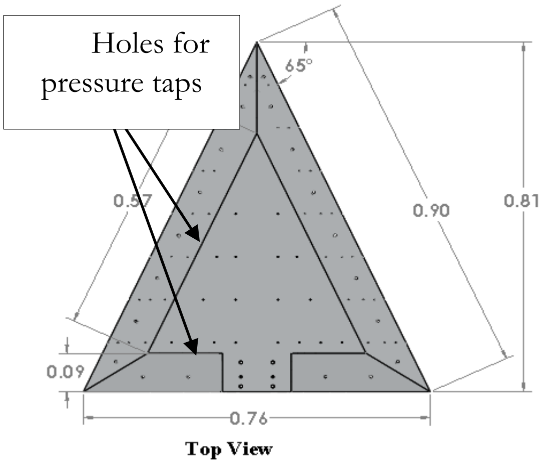

Figure 1: Dimensions of the VFE-2 delta wing model used in this study

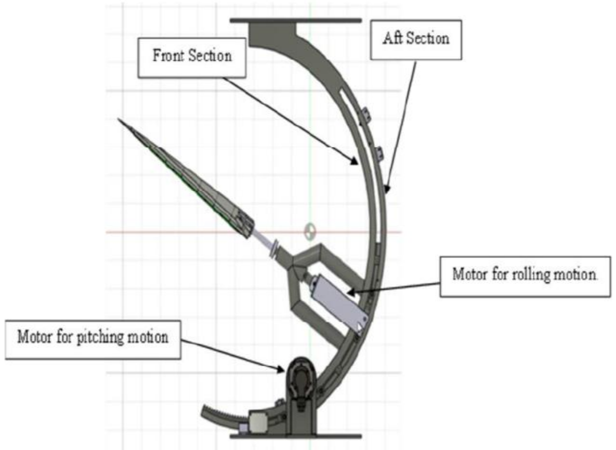

Figure 2: Wind tunnel test rig assembly for this study

The surface pressure measurements were obtained using 106 pressure taps, which were distributed across the delta wing surface to capture the detailed pressure distribution as shown in previous Figure 1. Each pressure tap was connected through flexible tubing to a 128-channel pressure scanner (accuracy of ±0.05% full-scale), interfaced with LABVIEW for real-time data acquisition as depicted in Figure 3. Moreover, the tunnel free-stream velocity was measured using a Pitot-static tube that was connected to a digital manometer. The operating temperature and static pressure were also recorded to calculate air density and viscosity. The Reynolds number for the wind tunnel tests was set at 1.288×10^6, which was corresponding to a free-stream velocity of 25 m/s at 27 °C and 1 atm.

Figure 3: LABVIEW interface for real-time data acquisition process

The experiments were carried out at angles of attack ranging from 0° to 20°, with roll angles varied systematically to study the unsteady aerodynamic behavior. Each test condition was repeated three times to ensure consistency and reproducibility. Pressure data were recorded through LABVIEW and stored in Excel for further processing. The Reynolds number, Re was computed using the relation in Equation 1, where ρ is air density, V is free-stream velocity, L is chord length and μ is dynamic viscosity. Both air density and viscosity were determined through the data interpolation from standard air property tables at temperature, T equals 27 °C. Furthermore, the surface pressure data were then processed to compute the pressure coefficient, C_p that is defined by Equation 2, where P_s is surface static pressure, P_∞ is free-stream static pressure, ρ_∞ is air density and V_∞ is the free-stream velocity.

$$R_e = \frac{\rho V L}{\mu} \tag{1}$$

$$C_p = \frac{P_s - P_\infty}{0.5\rho_\infty V_\infty^2} \tag{2}$$

The averaged C_p values were later sorted in an Excel spreadsheet for clarity. Subsequently, Kriging interpolation was applied using the Surfer software to estimate the C_p distributions across the delta wing surface. It should be noted that the Kriging method accounts for spatial correlations between pressure tap locations, producing smooth contour maps of the pressure distribution. In order to refine the results of the wind tunnel testing, correction methods can be applied. The tunnel blockage effects have been considered as the influence of the solid walls surrounding the finite tunnel flow on the flow field at the model [9]. For this study, the Maskell's correction [10] for tunnel blockage effects was applied.

Uncertainty analysis was also performed to quantify the reliability of the experimental results. The pressure scanner provided a measurement accuracy of ± 0.05% full scale whereas the Pitot-static tube velocity measurements had an uncertainty of ± 0.2 m/s. On the other hand, the angular positioning system allowed adjustment of angle of attack and roll with a tolerance of ± 0.1°. Repeatability checks were conducted by repeating each test condition three times and the standard deviation of C_p values was calculated to estimate the experimental scatter. Overall, the propagation of uncertainty through the C_p equation indicated a combined error of less than ± 2%. This level of accuracy was deemed sufficient for capturing aerodynamic trends of the delta wing under dynamic motions.

All in all, Figure 4 outlines the overall methodological framework for this study.

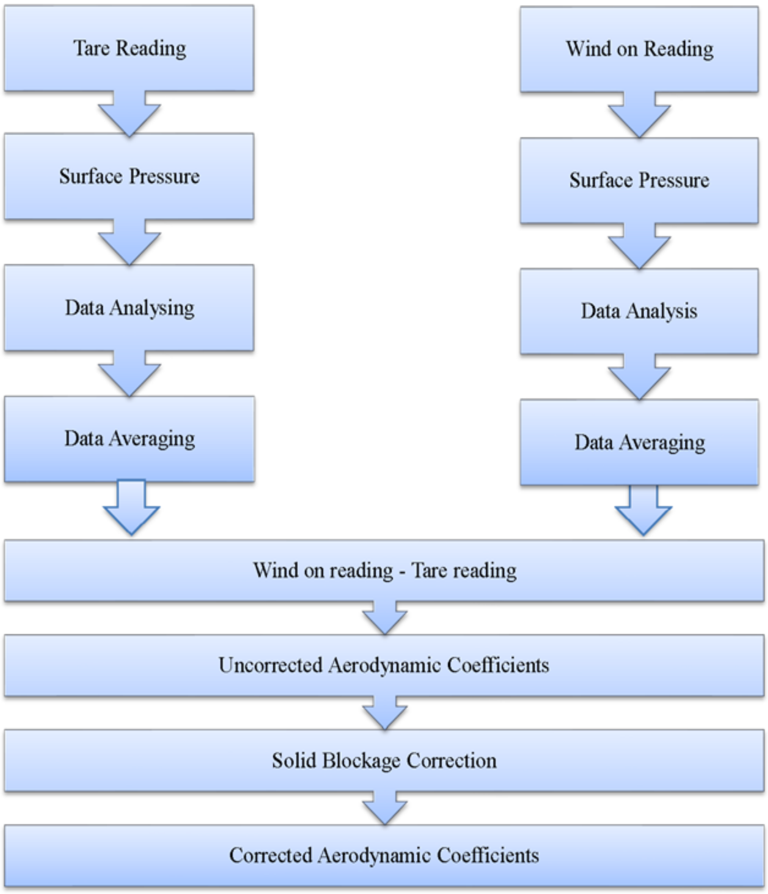

Figure 4: Overall flowchart of data collection and analysis process in this study

3. Results and Discussion

The pressure distribution in a pitching motion on the VFE-2 delta wing was investigated at angles of attack, AOA ranging from 0° to 20°. At 0°, the C_p distribution appears to remain relatively uniform, indicating the absence of any significant vortex activity. However, as AOA increased to 10°, the pressure distribution revealed the onset of the leading-edge vortex formation, which was characterized by lower pressure regions near the leading edges. This situation can be observed in Figure 5.

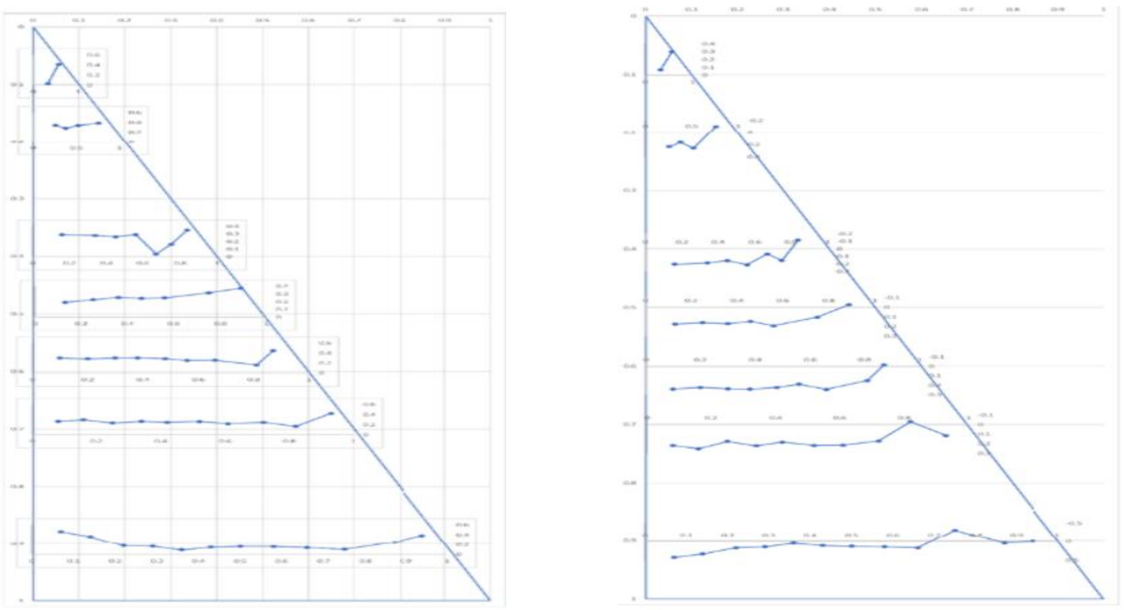

(a) AOA = 0°

(b) AOA = 5°

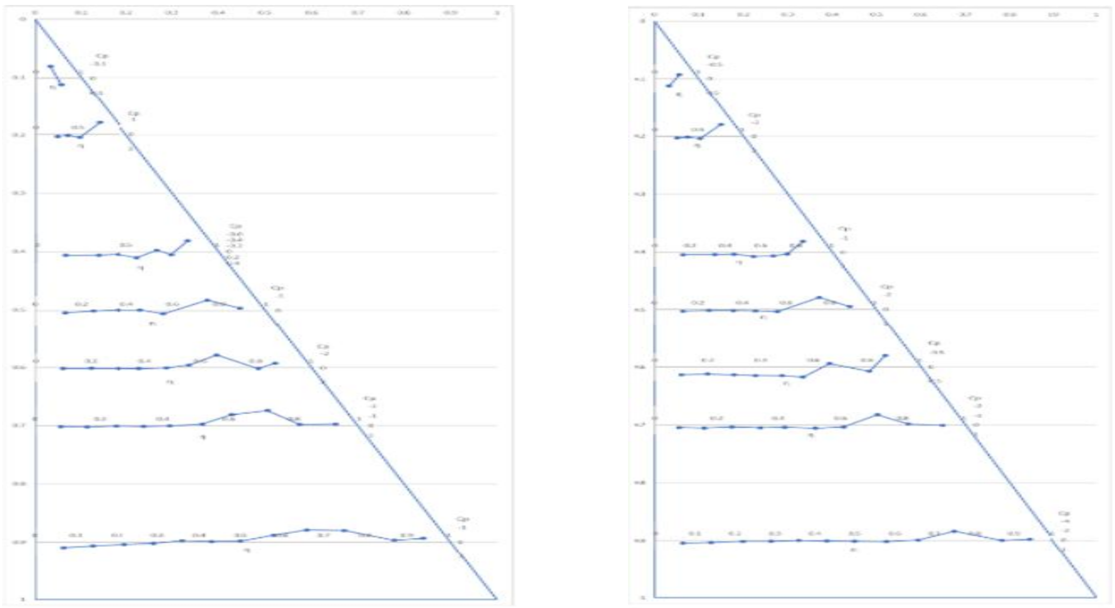

(c) AOA = 8°

(d) AOA = 10°

Figure 5: Effect of vortex formation at AOA between 0° to 10°

Furthermore, Figure 6 depicts the effects of vortex formation for the delta wing between angles of attack of 13° to 20°. At 15°, stronger suction peaks were observed along the leading edges, suggesting well-developed primary vortices. When the AOA reached 20°, the suction peaks had further intensified and extended upstream, highlighting the growth of the primary vortex system and the early emergence of the secondary vortices. These results demonstrate the progressive development of vortex-dominated flow as AOA increased. On the whole, at low AOA (i.e. between 0° to 5°), the flow remained attached with negligible vortex activity. By 10°, coherent leading-edge vortices were established, resulting in the distinct low-pressure regions. At 15°, the vortices strengthened significantly, accompanied by the wider suction footprint across the wing surface. Eventually, at 20°, the flow exhibited more complex patterns, including the development of secondary vortices closer to the wing root.

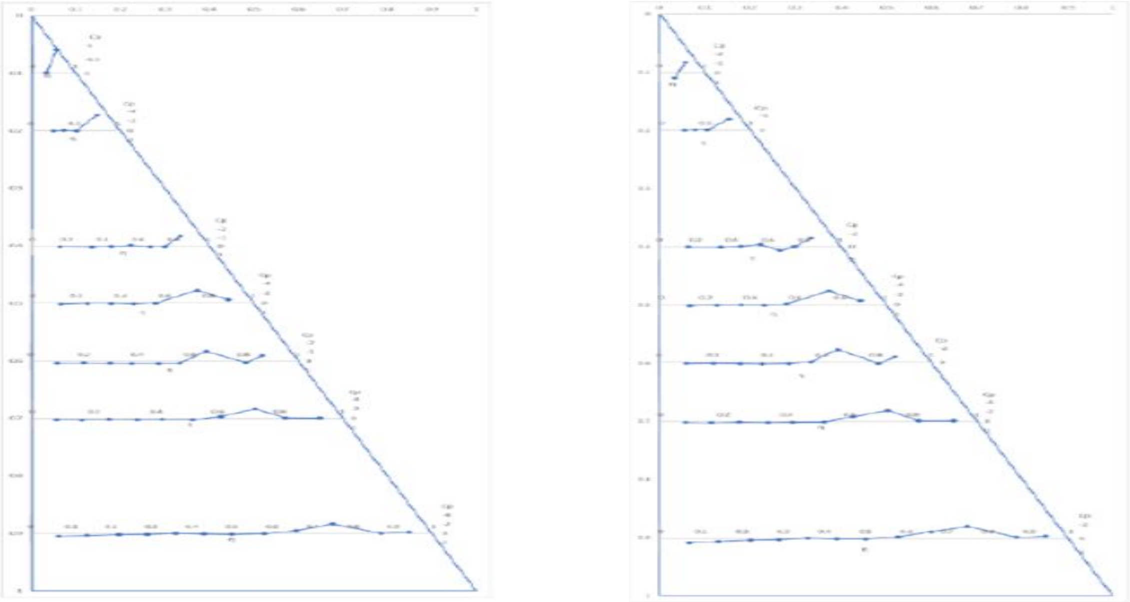

(a) AOA = 13° (b) AOA = 15°

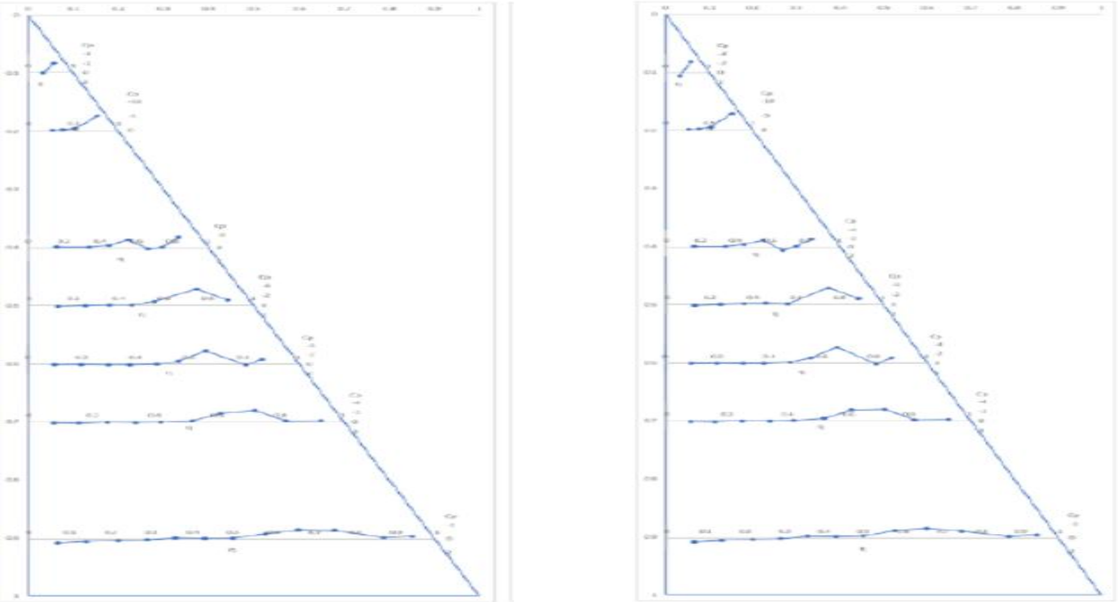

(c) AOA = 18° (d) AOA = 20°

Figure 6: Effect of vortex formation at AOA between 13° to 20°

The obtained results confirm that both the vortex's strength and position are strongly dependent on the AOA. As the AOA increased, the primary vortex moved upstream and closer to the wing surface. In addition, the secondary vortex structures emerged, consistent with the aerodynamic behavior of the delta wing as reported in the previous studies. The flow topology was further examined using pressure contours interpolated with the Kriging method. This approach allowed detailed visualization of pressure distributions across the wing surface beyond the limits of the discrete pressure tap measurements. The contour plots, as shown in Figure 7, demonstrated that at higher AOAs, the suction region expanded toward the root and shifted upstream. At 20°, the contours indicated a progressive upstream migration of both primary and secondary vortex cores. The use of the Kriging interpolation provided continuous representations of the pressure field, thereby enhancing the interpretation of the vortex interaction and breakdown phenomena.

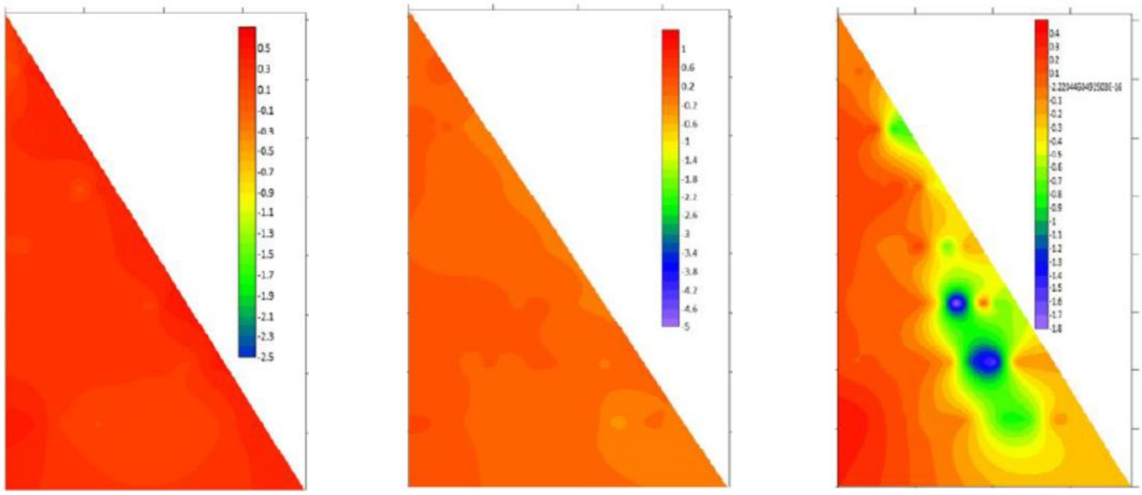

(a) AOA = 0° (b) AOA = 5° (c) AOA = 8°

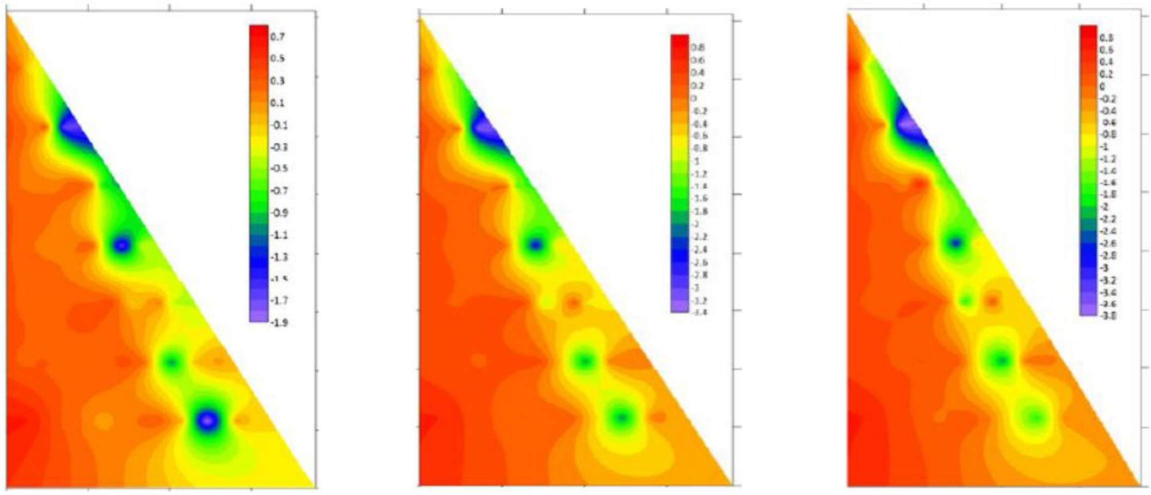

(d) AOA = 10° (e) AOA = 13° (f) AOA = 15°

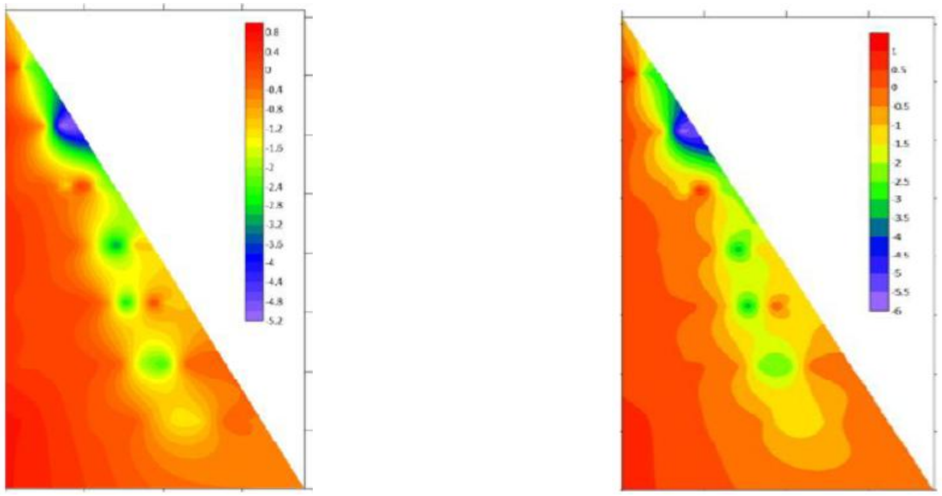

(g) AOA = 18° (h) AOA = 20°

Figure 7: Flow topology at AOA ranging between 0° to 20°

All in all, the experimental findings highlighted several key aerodynamic characteristics of the VFE-2 delta wing as listed as follow:

- **Primary vortex development:** Initiated at moderate AOA (≈10°), intensifying with the increasing angle.
- **Upstream shift:** At higher AOAs, the primary vortex migrated upstream and moved closer to the wing surface.
- **Secondary vortex formation:** The secondary vortices emerged at 20°, contributing to the increased flow complexity.
- **Vortex breakdown tendency:** The upstream shift and intensification of vortices at 20° suggest the onset of vortex breakdown, consistent with delta wing flow theory.

Overall, the results align with previous aerodynamic studies, confirming that the sharp-edged delta wing maintains strong vortex lift at high AOAs but also prone to the flow instability and breakdown at extreme conditions.

In the meantime, for rolling motions, Figure 8 shows the experimental results for the sharp-edged delta wing subjected to a constant roll angle, Φ of 10° and AOA ranging from 0° to 20°. Freestream pressure was used as the reference condition across all experiments, serving as the tare values for data normalization. The results are discussed in terms of C_p distributions and contour plots to highlight the influence of angle of attack and rolling motion on the flow behavior. In Figure 8, at AOA of 0°, the C_p distribution across the span appears to be nearly symmetric. A slight increase in pressure occurred near the nose whereas the gradual decrement towards the tips resulted in small negative C_p values. With the application of roll, the outer wing showed marginally lower pressure while the inner wing experienced a higher pressure. The resulting asymmetry was weak but established the basis of roll-induced pressure differentials. When AOA was 5°, suction increased near the leading edge and the outer wingtip showed stronger negative C_p while the inner wing retained higher pressure. At AOA of 8°, the low-pressure region expanded, appearing earlier along the chord ($x/c \approx 0.2$). Moreover, at AOA of 10°, the pressure asymmetry further intensified, with the outer wingtip experiencing the maximum suction and the inner wing showing elevated positive pressure. These indicated the strengthening of the leading-edge vortices with increasing incidence, amplified by the roll-induced inclination. Furthermore, at AOA of 13°, the pressure distributions revealed sharp reductions near the leading edge ($x/c = 0.2$ to 0.4). This behavior was in correspondent to the development of the coherent leading-edge vortices, which sustained lift by generating strong suction above the wing. A slight pressure recovery is observed near the trailing edge, linked to wake formation. The contours confirmed an enhanced vortex activity, with strong asymmetry between the outer and inner wing. Moving to when AOA was 15°, strong suction at the nose ($x/c \approx 0.1$) signified a vortex-dominated flow. This condition coincided with the onset of vortex breakdown reported for sharp-edged delta wings at high Reynolds numbers. The contours revealed enlarged low-pressure regions, particularly on the outer wing due to the rolling motion. At AOA of 18°, the negative pressure peak reduced slightly despite the higher incidence, suggesting the destabilization of the leading-edge vortices. Rolling further sheared the vortex structures, producing broader but less coherent low-pressure regions. Finally, at the maximum tested incidence where AOA was 20°, the pressure coefficient reached its lowest values across the wing. Extensive low-pressure regions in the contour plots marked the vortex breakdown and collapse. This stage was associated with the significant lift loss and increased drag, representing severe aerodynamic instability. Across the tested range, three different regimes can be identified as listed below:

- **Low incidence (i.e. AOA < 5°)** – nearly symmetric distributions, weak roll effect.
- **Moderate incidence (i.e. AOA between 5° and 10°)** – strong suction, coherent vortices, roll-induced asymmetry.
- **High incidence (i.e. AOA ≥ 13°)** – vortex-dominated flow transitioning into breakdown; rolling accelerates asymmetry and destabilization.

Overall, the rolling motion at $\Phi = 10°$ can be seen to consistently enhance the pressure asymmetry across the wingspan. While this contributes to the roll control effectiveness at moderate AOA, it also accelerates vortex breakdown at higher incidence, degrading aerodynamic stability.

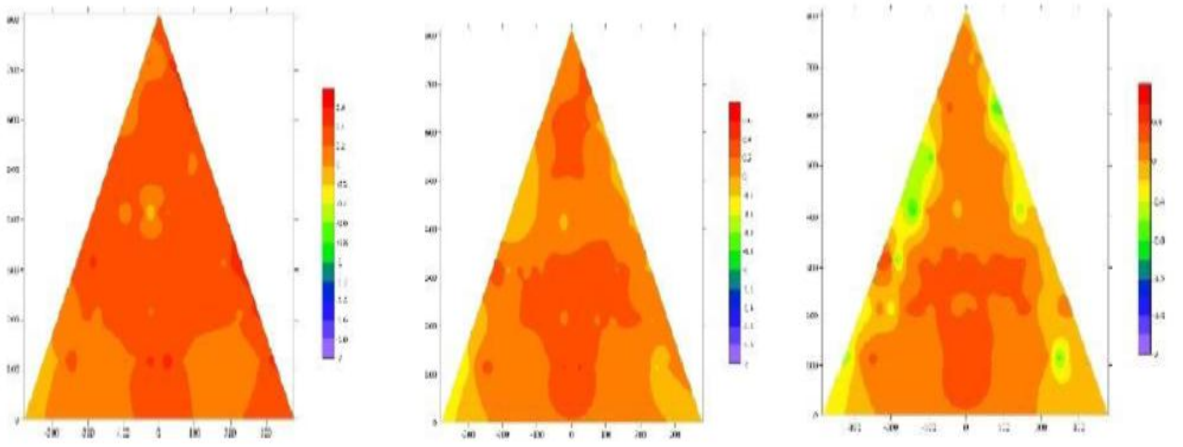

(a) AOA = 0° (b) AOA = 5° (c) AOA = 8°

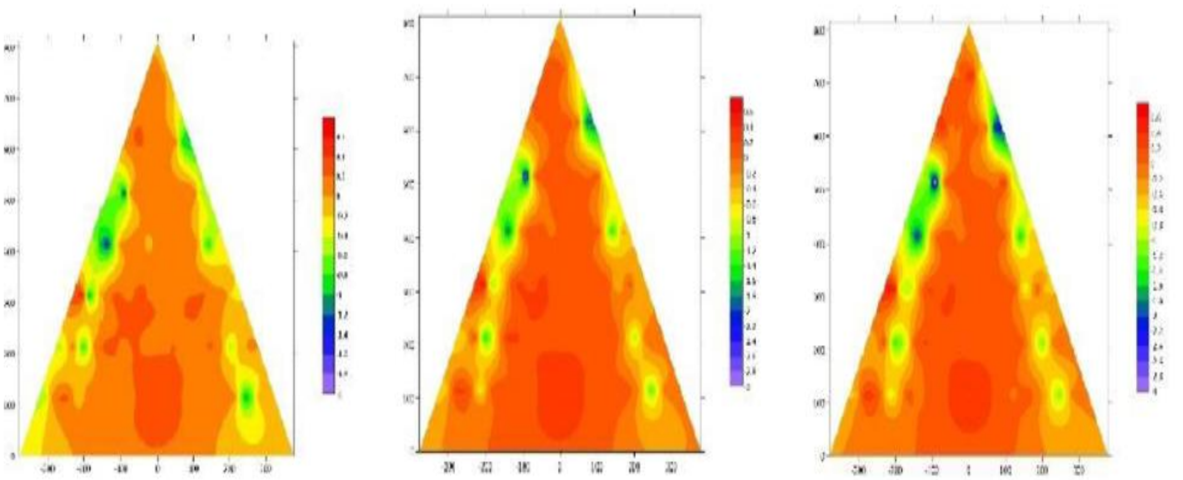

(d) AOA = 10° (e) AOA = 13° (f) AOA = 15°

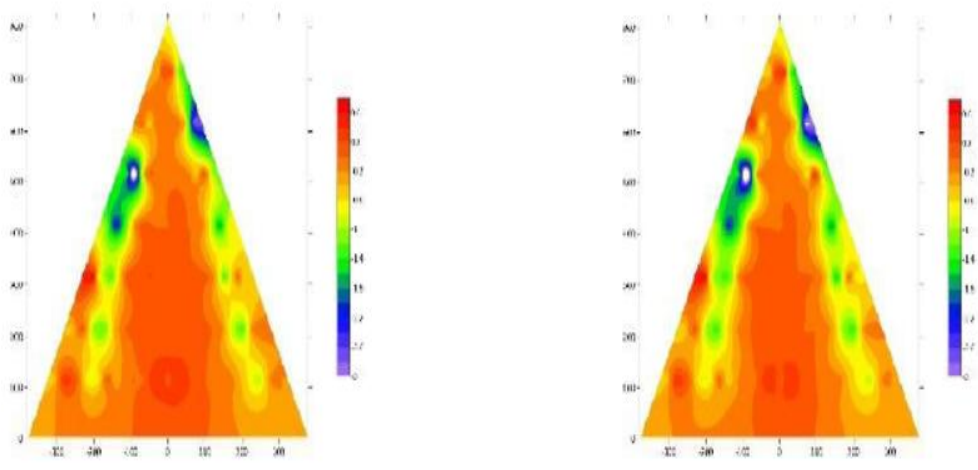

(g) AOA = 18° (h) AOA = 20°

Figure 8: Pressure coefficient characteristics at different AOA for Φ = 10°

4. Conclusion

This study experimentally investigated the aerodynamic behavior of the sharp-edged VFE-2 delta wing under both pitching and rolling motions. The results have provided important insights into the effects of AOA and dynamic motion on the vortex flow topology, pressure distribution and the overall aerodynamic performance. For the pitching motion experiments, the findings have demonstrated that AOA has dominant influence on the vortex development. At lower AOAs (i.e. AOA $\leq 5°$), the flow remained attached with minimal vortex activity. With increasing AOA, flow separation initiated at the leading edge, forming the primary vortices whose position and strength evolved along the chord. The primary vortex strengthened and moved upstream with higher AOA while vortex breakdown occurred at the trailing edge for high AOAs (i.e. AOA $\geq 18°$). Weak secondary vortices were observed in some cases, particularly at AOA of 8°, 18° and 20°. The conducted pressure contour analyses confirmed that vortex strength and breakdown location are closely linked to AOA, with the breakdown characterized by the disappearance of suction peaks and loss of coherent vortex structure. Meanwhile, for the rolling motion case at Φ of 10°, the pressure coefficient was observed to decrease as AOA increased due to the destabilization and breakdown of the leading-edge vortices. Rolling motion amplified asymmetries in the vortex system, making breakdown more likely even at moderate AOA. The reduction in lift and increase in drag were attributed to vortex disruption and wake formation. Differences in the pressure coefficient were more pronounced at higher AOA, indicating that the rolling motion strongly influences vortex stability. On the whole, from a design perspective, these results suggest that sharp-edged delta wings exhibit stable vortex behavior at the lower AOA under both pitching and rolling motions. Stable operation has been observed up to approximately AOA of 8° at 25 m/s of free-stream velocity. Beyond this range, vortex breakdown dominates the flow, leading to aerodynamic performance penalties. These findings provide valuable guidance for the aerodynamic design and control of delta-wing configurations operating in dynamic flight conditions.

Acknowledgement

The authors would like to thank the Aeronautics Laboratory, Universiti Teknologi Malaysia (UTM) for their support in this research activity.

References

[1] I. Gursul, 'Review of Unsteady Vortex Flows Over Delta Wings', Presented at AIAA Applied Aerodynamics Conference, Orlando, USA, 2003.

[2] I. Gursul, R. Gordnier and M. Visbal, 'Unsteady Aerodynamics of Nonslender Delta Wings', Progress in Aerospace Sciences, vol. 41, no. 7, pp. 515-557, 2005.

[3] M. F. A. Zamzuddin, M. Said, N. A. Musa, K. A. Kasim and S. Mat, 'Analysis of Vortex on Sharp-edged Delta Wing with Blowing Effect', Journal of Transport System Engineering, vol. 10, no. 1, pp. 14-23, 2023.

[4] M. V. Lowson and A. J. Riley, 'Vortex Breakdown Control by Delta Wing Geometry', Journal of Aircraft, vol. 32, no. 4, pp. 832-838, 1995.

[5] I. Gursul and C. M. Ho, 'Vortex Breakdown Over Delta Wings in Unsteady Freestream', AIAA Journal, vol. 32, no. 2, pp. 433-436, 1994.

[6] M. Sereez, M. Goman, N. Abramov and C. Lambert, 'Numerical Simulation of Self-Sustained Roll Oscillations of an 80-Degree Delta Wing Caused by Leading-Edge Vortices', Aerospace, vol. 12, no. 3, 197, 2025.

[7] V. Kumar, A. C. Mandal and K. Poddar, 'An Experimental Investigation on the Aerodynamic Characteristics and Vortex Dynamics of a Flying Wing', The Aeronautical Journal, vol. 128, no. 1326, pp. 1681-1705, 2024.

[8] I. Gursul, R. Gordnier and M. Visbal, ‘Unsteady Aerodynamics of Nonslender Delta Wings’, Progress in Aerospace Sciences, vol. 41, no. 7, pp. 515-557, 2005.
[9] S. Wiriadidjaja, A. S. Mohd Rafie, F. I. Romli and O. K. Ariff, ‘Aerodynamic Interference Correction Methods Case: Subsonic Closed Wind Tunnels’, Applied Mechanics and Materials, vol. 225, pp. 60-66, 2012.
[10] J. E. Hackett and K. R. Cooper, ‘Extensions to Maskell’s Theory for Blockage Effects on Bluff Bodies in a Closed Wind Tunnel’, The Aeronautical Journal, vol. 105, no. 1050, pp. 409-418, 2001.

JOURNAL OF AEROSPACE SOCIETY MALAYSIA

GAP EFFECT ON AERODYNAMIC PERFORMANCE OF A FLAT PLATE WITH FORE AND AFT EMBEDDED ROTATING CYLINDERS

Hidayatullah Mohammad Ali [1], * and Azmin Shakrine Mohd Rafie [1]

1. Department of Aerospace Engineering, Faculty of Engineering, Universiti Putra Malaysia, 43400 Serdang, Selangor, Malaysia.

*Correspondence: hidayatullah@upm.edu.my

Abstract: Boundary layer separation significantly affects aerodynamic performance of airfoils, turbine blades and flat plates, which reduces lift at high angles of attack and limits the efficiency in applications such as unmanned aerial vehicles (UAVs). A promising approach to delay the separation and enhance lift is the use of rotating cylinder near the surface, which leverages Magnus effect to inject momentum into the boundary layer. This study investigates the aerodynamic performance of a flat plate embedded with fore and aft rotating cylinder (CyFlaP), with particular emphasis on the influence of the gap size between the cylinders and the plate. The main objective is to identify the optimal gap configuration for maximizing lift coefficient (C_L) while ensuring flow stability across different Reynolds number regimes. Two-dimensional computational fluid dynamics (CFD) simulations were conducted in ANSYS Fluent, employing the SST $k - \omega$ turbulence model. For the analysis, the gap variation is from 1 mm to 10 mm while the inflow velocities ranging from 5 m/s to 30 m/s as these ranges capture the practical operating conditions and allow evaluation of their influence on the aerodynamic performance. A structured mesh with validated grid independence was used and the transient solver settings captured unsteady vortex dynamics around the rotating cylinders and flat plate. Results indicate that narrow gaps of 1 mm to 2 mm achieved the highest lift, with coefficients exceeding 3.7 at 20 degrees angle of attack for 5 m/s, corresponding up to 9% improvement over wider gaps. Nevertheless, this advantage diminished with increasing velocity, where wider gaps consistently underperformed and all configurations converged to C_L less than 1.4 at 25 m/s to 30 m/s. On the whole, the study concludes that gap tuning is most effective at low to moderate Reynolds numbers, with 1 mm identified as optimal and 2 mm to 3 mm offering a practical compromise for UAV applications. This effectiveness arises because smaller gaps enhance the momentum injection into the boundary layer, strengthening circulation around the plate and delaying flow separation while slightly larger gaps maintain lift enhancement without excessive viscous losses.

Keywords: boundary layer separation, computational fluid dynamics, gap variation, Magnus effect, unmanned aerial vehicle

1. Introduction

Boundary layer separation plays a critical role in determining aerodynamic performance in devices such as airfoils, turbine blades and flat plates [1]. At high angles of attack (α), flow separation over the upper surface reduces lift, leading to a lower lift coefficient (C_L) and impaired aerodynamic efficiency [2]. Delaying the separation of the boundary layer, which is the point where airflow detaches from the surface, is therefore essential, particularly in applications like unmanned aerial vehicles (UAVs) where maintaining attached flow helps to maximize lift without excessive weight or energy consumption. One effective method to enhance lift is momentum injection using a rotating cylinder near the surface of the body [3]. This mechanism is directly linked to the Magnus effect, in which a rotating body in a fluid generates lift due to pressure differences around its surface [4]. The Magnus effect essentially provides the fundamental physical explanation for the lift benefits of rotating cylinders and is highly relevant for modern UAV designs.

In 1925, the application of a rotating cylinder embedment onto bluff geometry existed all the way back then [5]. The rotating cylinder embedment on the flat plate (CyFlaP) are influenced significantly by a past research work known as Leading Edge Cylinder Airfoil (LECA). In fact, the theory of LECA was first tested by Wolf [5] and Wolf and Koning [6] in 1925 and 1926, respectively, which resulted in enormous results for its aerodynamic performance. Till then, in 2014, Ahmed et al. [7] conducted a numerical analysis of a NACA 0024 airfoil with a rotating cylinder mounted at the leading edge using ANSYS CFX under the transient conditions and the SST turbulence model. Their study compared the modified airfoil with the baseline unmodified airfoil and reported that C_L of modified airfoil increased by 36% while its stall angle was delayed by 122%. This improvement in lift occurred because the rotating cylinder injected momentum into the boundary layer, strengthening circulation over the upper surface and delaying flow separation at higher angles of attack. The enhanced aerodynamic collectively indicates that leading edge cylinder rotation significantly improves the aerodynamic performance of the airfoil. Conversely, in 2015, Huda et al. [8] studied the LECA embedment onto NACA 0010 and produced the maximum model lift of 145% better than its unmodified model, thereafter delaying the separation flow at a higher momentum injection from the rotating cylinder. Moreover, recent research by Ali et al. [9] in 2021 demonstrated that CyFlaP could achieve up to a 76% increase in C_L compared to an unmodified flat plate. In 2022, Ali et al. [10] validated the concept on the Selig S1223 airfoil, showing that the dual rotating cylinders significantly delayed stall and improved lift at high angles of attack. Azman et al. [11] in 2022 extended this work further by developing a UAV prototype based on the CyFlaP design, which generated a lift force of 62.65 N at a velocity of 21 m/s and supported a payload of approximately 6.4 kN. While these studies confirmed the lift-generating potential, they also highlighted the importance of cylinder placement and rotation speed in maximizing lift performance.

A key parameter influencing lift in the CyFlaP system is the gap between the rotating cylinder and the flat plate. In 2017, Abdulla and Hasan [12] have numerically investigated on the effect of gap and found that the gap space of 3 mm was best for their study. They also denoted that the separation of the model at higher α did not appear as compared to the one without cylinder embedment. They concluded that the effect of gap has resulted with 35% and 21% better in lift and drag coefficients, respectively. The gap affects the momentum transferred into the boundary layer and subsequently the ability of the cylinder to control separation. Optimizing the gap is essential because an improperly sized gap could disturb the boundary layer, trigger premature flow separation and reduce the maximum achievable lift [13]. Modern computational studies allow systematic investigation of gap sizes, providing insights into how gap variation influences boundary layer behavior and lift generation. Further studies demonstrated that cylinder rotation speed and placement significantly affect the lift enhancement. Kamid et al. [14], Roslan et al. [15] and Zaimi et al. [16] have reported that higher rotational speed combined with optimal cylinder positioning suppress flow separation and stabilize unsteady flow structures, thereby increasing C_L. Additional bluff-body flow control strategies such as base bleed [17], top plate [18], end plates [19], splitter plates [20], secondary cylinders [21] and also sharp-edged flat tabs [22], have been explored to further improve lift and flow stability. However, unlike these auxiliary modifications, the gap in the CyFlaP configuration is an intrinsic design feature, hence its optimization is critical for the effective lift enhancement.

The CyFlaP flat plate also provides a controlled environment for examining the fundamental flow phenomena, including boundary layer behavior, vortex formation and unsteady wake structures. By systematically varying the gap size, it is possible to quantify how the momentum injection modifies the flow, delays separation and maximizes lift at different angles of attack. Insights from these analyses are highly relevant to the UAV design, where energy-efficient, lightweight and high-lift surfaces are essential for high-altitude operation. In this study, computational fluid dynamics (CFD) using ANSYS Fluent is employed to perform two-dimensional simulations of CyFlaP configurations with the gap sizes ranging from 1 mm to 10 mm. The simulations aim to determine how the gap variation influences C_L and to identify optimal conditions for maximizing momentum transfer into the boundary layer. The findings provide a design guidance for high-lift UAV and contribute to a better understanding of unsteady flow dynamics in rotating-cylinder systems. By integrating the Magnus effect, CFD simulations and a detailed parametric analysis of gap size, this work seeks to enhance lift generation and provide practical insights for UAV and high-altitude platform design. The focus on gap optimization aligns the study with current technological needs and ensures relevance for both applied and fundamental aerodynamic research.

2. Methodology

The present study employs CFD to analyze the aerodynamic performance of a flat plate embedded with fore and aft rotating cylinders, with emphasis on the influence of gap variation. The computational procedure followed a structured approach, beginning with geometry generation, followed by turbulence model selection, mesh generation, solver configuration and validation through a mesh independency test. It can be noted that this methodology has been widely adopted in prior aerodynamic investigations to ensure reliability and reproducibility of CFD results [23].

2.1 Geometry configurations

The rotating cylinders form the foundation of CyFlaP configuration. Badalamenti [24] investigated the aerodynamic performance using wind tunnel testing at City University's Handley Page Aerodynamic Laboratory, validating the effects of cylinder rotation on flow control. The experimental results were consistent with Betz's theoretical work, which identified an aspect ratio (AR) of 4.7 as significant for the aerodynamic scaling [25]. For this study, the cylinder dimension follows Badalamenti's configuration with an applied AR of 5.1. Each cylinder has a diameter of 0.16 m and is rotated clockwise, consistent with Badalamenti [24]. Clockwise rotation accelerated the flow above the cylinder and decelerated it below, thereby generating an upward Magnus lift force as noted by Barati et al. [26]. The schematic of the rotating cylinder is shown in Figure 1.

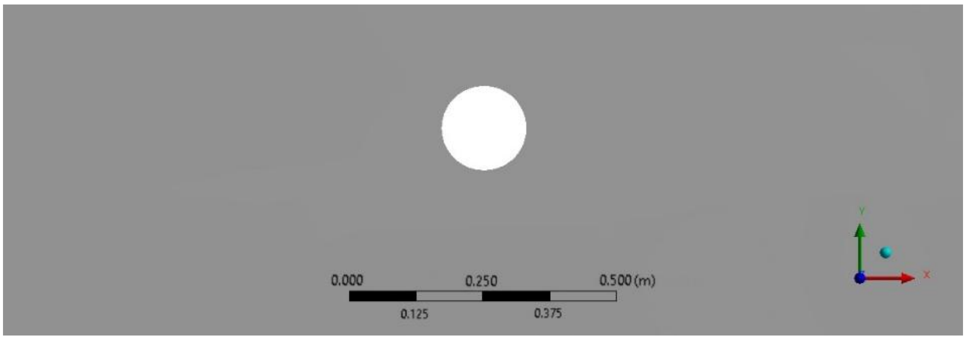

Figure 1: Rotating cylinder schematic diagram

The flat plate serves as the baseline aerodynamic surface onto which the cylinders are embedded. Its aerodynamic simplicity and effectiveness have been highlighted by Wang et al. [27] and Torres and Mueller [28], who demonstrated that flat plates can sustain high α, achieving up to 60% of the maximum lift coefficient (C_{Lmax}) of conventional airfoils. For this study, the flat plate has a chord length of 1 m. The schematic of the flat plate baseline is shown in Figure 2.

The combined CyFlaP configuration was first proposed by Modi [29], originally to reduce drag in bluff bodies such as trucks. In Modi's early work, the rotating cylinders were mounted close to the bluff-body surfaces primarily for drag reduction, but the exact gap between the cylinder and surface was not systematically varied or optimized as the configuration emphasized the qualitative flow control rather than the parametric gap studies. Later studies extended its application to the lift enhancement by embedding rotating cylinders along the camber line of the flat plate. In this arrangement, cylinders are positioned at the leading edge and trailing edges with a defined separation gap from the plate surface. Abdulla and Hasan [12] demonstrated that the gap strongly influences aerodynamic performance, with intermediate values yielding optimal lift-to-drag ratios. Specifically, Abdulla and Hasan [12] investigated gap sizes of 1 mm, 2 mm, 3 mm, 4 mm and 5 mm for embedded rotating cylinder at the leading edge of a NACA 0012 airfoil and identified the 3 mm gap as the optimum configuration across velocity ratios ($U_C/U_\infty = 1$ to 3). In this study, the gap sizes ranging from 1 mm to 10 mm are investigated to examine their effect on the momentum injection, separation delay and lift augmentation. Thus, the current work expands the explored parameter space by testing gaps up to 10 mm, considerably wider than the 1 mm to 5 mm range studied by Abdulla and Hasan [12], and by applying the CyFlaP concept to a flat plate configuration rather than the NACA 0012 airfoil geometry used previously. The CyFlaP geometry with embedded cylinders and gap variation is illustrated in Figure 3.

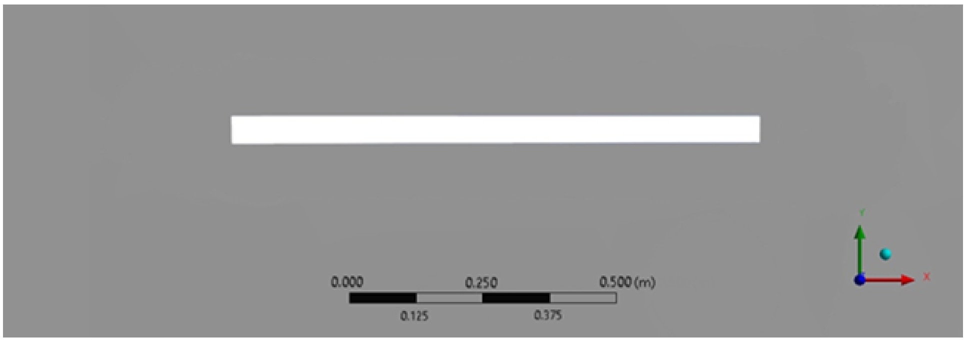

Figure 2: Flat plate schematic diagram

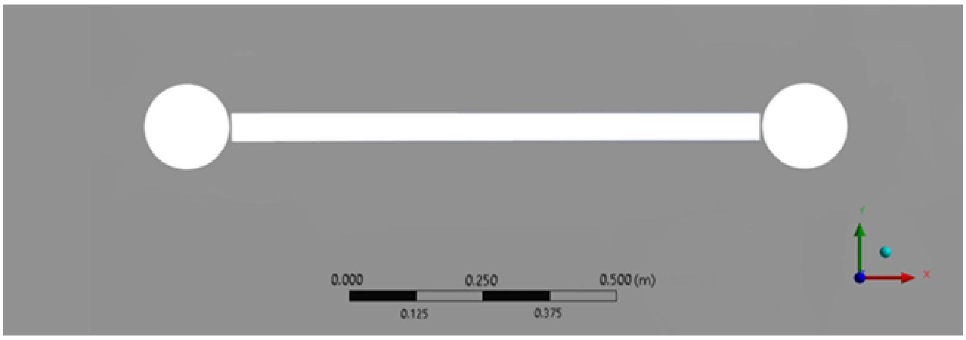

Figure 3: CyFlaP geometry with embedded cylinders and gap variation schematic diagram

2.2 Turbulence model

In general, the turbulence modelling provides a numerical approach to close the Reynolds-averaged Navier-Stokes (RANS) equations, enabling prediction of the turbulent flow effects through additional transport equations. In this study, the Shear Stress Transport (SST) $k - \omega$ model was selected, following its successful application in similar aerodynamic investigations by Ali et al. [9, 30] and Mgaidi et al. [31]. The two-equation model introduces the turbulent kinetic energy (k) as the first transported variable and the specific dissipation rate (ω) as the second variable, allowing accurate presentation of the turbulent transport properties.

The SST k – ω model was introduced by Menter [32] as improvement over Wilcox's original k – ω formulation [33]. Its formulation blends the advantages of the k – ω model in the near-wall region with the k – ω model in the far field, thereby reducing sensitivity to free-stream turbulence levels. This hybrid approach enhances predictive accuracy in flows with strong adverse pressure gradients and separation, which are central features of the CyFlaP configuration. The transport equations for the SST k – ω model are expressed as in Equation 1 and Equation 2.

$$\frac{\partial}{\partial t}(\rho k) + \frac{\partial}{\partial x_i}(\rho k u_i) = \frac{\partial}{\partial x_j}\left[\Gamma_k \frac{\partial k}{\partial x_j}\right] + G_k - Y_k + S_k \tag{1}$$

$$\frac{\partial}{\partial t}(\rho \omega) + \frac{\partial}{\partial x_i}(\rho \omega u_i) = \frac{\partial}{\partial x_j}\left[\Gamma_\omega \frac{\partial \omega}{\partial x_j}\right] + G_\omega - Y_\omega + S_\omega \tag{2}$$

Equation 1, which is transport equation for k, describes how turbulence is produced, transported and dissipated in the flow. In this equation, G_K represents the generation of turbulent kinetic energy due to mean velocity gradients, indicating how shear in the flow produces turbulence. Y_K denotes the dissipation of k into thermal energy due to viscous effects while Γ_K represents the effective diffusivity controlling the spatial transport of k. An additional source term, S_K allows user-defined contributions to turbulent kinetic energy if necessary. Similarly, the transport equation for ω in Equation 2 describes how the turbulence decay rate evolves in the flow. In this equation, G_ω represents the generation of ω due to the velocity gradients, Y_ω is the dissipation of ω and Γ_ω is the effective diffusivity controlling its transport. S_ω accounts for any user-defined sources for ω. Together, Equation 1 and Equation 2 provide a complete description of the production, diffusion, and dissipation of turbulence in the flow, allowing the SST k – ω model to accurately capture the near-wall behavior, flow separation, and unsteady vortical structures in the CyFlaP configuration.

2.3 Grid generation and mesh validation

The pre-processing stage of this research required the construction of a computational grid that properly defined the boundaries and ensured reliable two-dimensional (2D) numerical simulations. In CFD, grid generation is one of the most crucial steps as the accuracy of the numerical solution depends heavily on the mesh quality and the suitability of its configuration for capturing the governing Navier-Stokes equations. In line with the approaches of Mgaidi et al. [31] and Yao et al. [34], a block-structured mesh was adopted for this study to balance the computational efficiency with the solution fidelity. The computational domain was established using a double rectangular block arrangement, consisting of an inner block of 2D x 3D surrounding the model and an outer block of 6D x 15D extending further into the far-field as shown in Figure 4(a). Here, D denotes the diameter of the rotating cylinder, which serves as the reference length for domain scaling. To adequately capture near-wall effects, inflation layers were applied on the model surfaces, consisting of 15 layers with a growth rate of 1.2, ensuring a y-plus (y^+) value of less than 1 as shown in Figures 4(b) and 4(c). This configuration provided sufficient resolution of the boundary layer and allowed for consistent implementation of the wall function approach under the selected turbulence model.

In this study, wall functions were employed with the SST k – ω model to ensure numerical stability and to reduce excessive grid requirements, particularly in regions where strong curvature and cylinder rotation-generated shear could otherwise demand extremely fine near-wall resolution. The use of wall functions therefore enabled a practical balance between computational cost and accuracy. The standard automatic wall treatment provided in the solver, which switches between the low-Reynolds-number integration and wall functions depending on local y^+, was used to accommodate the fine mesh near the rotating cylinder while maintaining robust convergence in the far-field and less sensitive regions. The boundary conditions and mesh parameters employed in the setup are tabulated in Table 1 and Table 2.

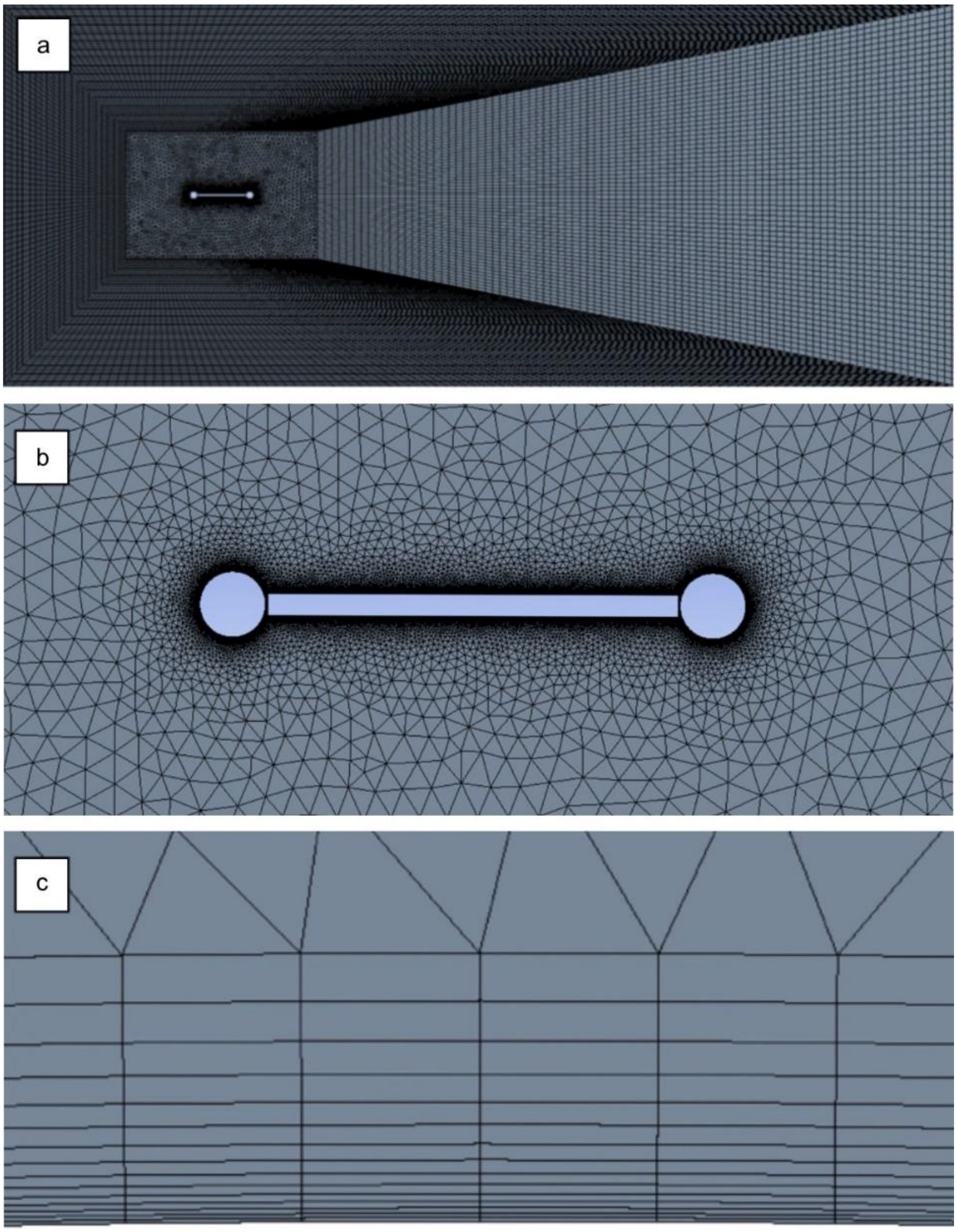

Figure 4: CyFlaP's computational setup showing: (a) domain configuration, (b) mesh generation near the model, (c) surface-body inflation layers

Table 1: Boundary conditions

Boundary conditions	Type
Inlet	Velocity-inlet
Outlet	Pressure-outlet
Cylinder	Wall
Selig airfoil	Wall
Wall	Symmetry
Interior surface body	Interior
Surface body	Interior

Table 2: Mesh setups

Mesh specifications	
Growth rate	1.2
Defeature size	5.e-004 m
Curvature minimum size	1.e-003 m
Curvature normal angle	18.0°
Smoothing	High
Inflation specifications	
Inflation option	First layer thickness
Maximum layers	15
Growth rate	1.2

The boundary condition strategy in this study followed the standard aerodynamic practice to ensure a realistic flow modelling. A velocity-inlet was specified at the upstream boundary to define the inflow velocity while pressure-outlet at the downstream boundary allowed smooth outflow without reflections. The cylinder and airfoil walls were treated as no-slip conditions to capture the viscous effects, with a symmetry boundary at the far-field wall to represent an unbounded domain. The interior surfaces were assigned as "Interior" to facilitate continuity between grid regions. The mesh specifications, including a growth rate of 1.2, defeature size of 5 x 10^{-4} m, curvature minimum size of 1 x 10^{-3} m and also high smoothing, were selected to maintain the accuracy in curved regions while ensuring overall numerical stability.

Before proceeding with the solver settings, a mesh independency test was performed to confirm the reliability of the grid and ensure solution independence from mesh density. Following the approach of Ali et al. [9] and Yao et al. [34], successive refinement of the grid was tested for both the rotating cylinder and the flat plate embedment configurations as depicted in Figure 5 and Figure 6, respectively. Two iterations of the mesh independency test were carried out and convergence of the C_L was observed at approximately 4.19 x 10^4 cells for the rotating cylinder and 9.19 x 10^4 cells for the flat plate. At these refinement levels, the error percentage fell below 1%, which confirmed that the selected mesh was both computationally efficient and also sufficiently accurate for capturing the required flow physics. This validated mesh configuration was therefore adopted for the subsequent CFD simulations.

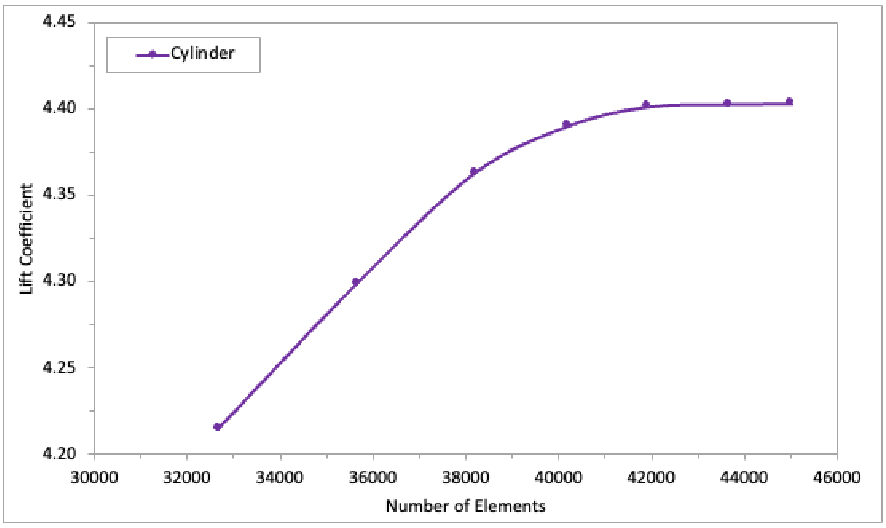

Figure 5: Cylinder's mesh independency test results

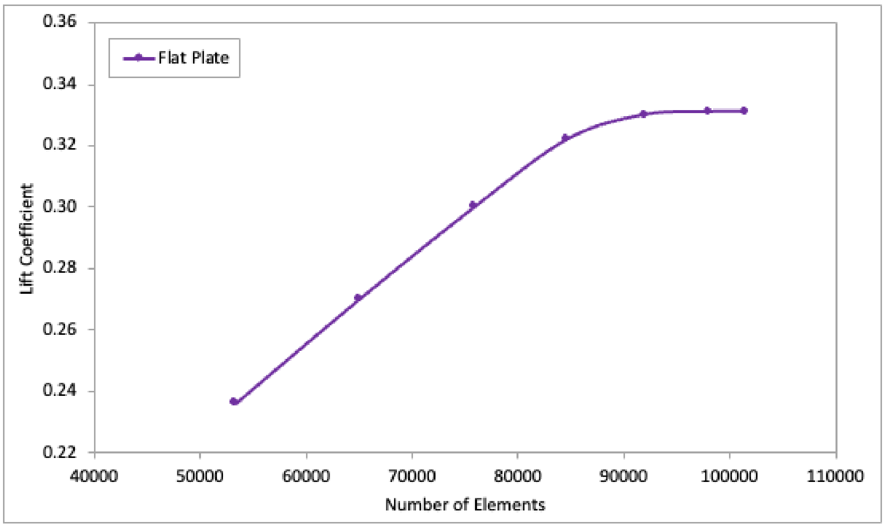

Figure 6: Flat plate's mesh independency test results

2.4 Solver setup

The numerical solution process relies heavily on the solver configuration, as it governs both the accuracy of the predictions and the stability of convergence. In this study, a pressure-based formulation was adopted, consistent with the incompressible and subsonic flow conditions of interest. A transient framework was employed to resolve the unsteady nature of the vortex shedding and the time-dependent interactions around the rotating cylinder and flat plate, which the steady-state models cannot adequately capture. To model the turbulence, the SST $k - \omega$ approach was applied, offering robust performance in resolving boundary-layer behaviour while retaining stability in the free-stream. This hybrid formulation is particularly effective for flows where separation and near-wall stresses play the decisive role in the aerodynamic performance. Reference values such as density, viscosity and freestream velocity were specified under the standard atmospheric conditions to ensure the physical consistency in evaluating aerodynamic characteristics across a range of operating speeds. The solution strategy employed coupled pressure-velocity iteration, a method that enhances the convergence reliability in flows with strong momentum-pressure interactions as in the case of rotating bodies. A stringent residual convergence criterion of 10^{-6} was enforced to maintain the solution fidelity throughout the computational domain. Spatial discretization schemes were selected to minimise numerical diffusion while preserving accuracy in regions with steep gradients.

The PRESTO! Algorithm was applied for pressure interpolation, offering superior resolution in swirling and rotational flows, while the QUICK scheme was used for momentum, turbulent kinetic energy and specific dissipation rate equations to capture the convection-dominated transport without excessive artificial smoothing. Gradient calculations relied on the Green-Gauss node-based method, ensuring a sharp resolution at interfaces and curved surfaces. Together, the solver setting provided a balance of computational efficiency and predictive accuracy, tailored to capture the complex unsteady aerodynamics central to this investigation.

2.5 Validation

A validation study was conducted for both the rotating cylinder and the flat plate prior to advancing with the CFD simulations as illustrated in Figure 7 and Figure 8, respectively. Particular attention was given to the embedding of these geometries within the computational domain to ensure the consistency with experimental configurations. The experimental investigations reported by Badalamenti and Prince

[24] and Torres and Mueller [28] provided the reference data for comparison, against which the present CFD results were assessed. The validation demonstrated good agreement, with discrepancies remaining within 10%, thereby confirming the reliability of the numerical setup for subsequent analysis.

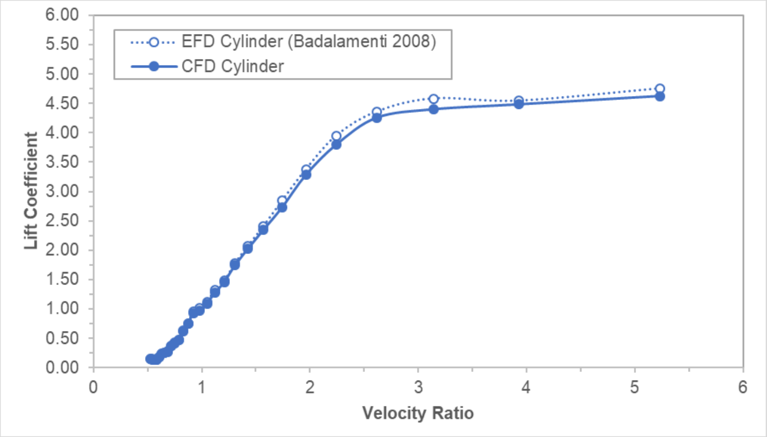

Figure 7: Cylinder's validation results

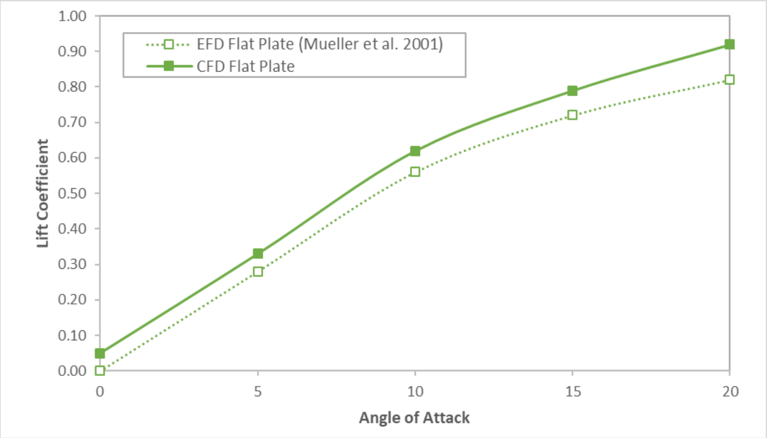

Figure 8: Flat plate's validation results

3. Results and Discussion

The aerodynamic behavior of the CyFlaP configuration was further examined by analyzing the C_L variations across a range of free-stream velocities, gap sizes and velocity ratios (V_r). The dataset was systematically organized into six sets, corresponding to the inflow velocities of 5, 10, 15, 20, 25 and 30 m/s. Within each velocity set, the effect of the gap size, ranging from 1 mm to 10 mm, was evaluated against V_r values from 0 to 20. This approach enables a detailed understanding of how flow separation, circulation and interaction between the cylinder and flat plate evolve within changing geometric spacing and dynamic conditions. By comparing these results, quantitative trends can be highlighted, identifying the gap configurations and operating conditions that maximize aerodynamic performance.

At free-stream velocity of 5 m/s, corresponding to Reynolds number of 456,140, the C_L showed a consistent upward trend with increasing angle of attack for all gap sizes between 1 mm and 10 mm, as shown in Figure 9. At zero degrees, C_L values ranged from 2.39 at 10 mm to 2.97 at 2 mm, indicating that smaller gaps promoted a stronger lift generation at low incidence. As the angle of attack increased to 20 degrees, C_L peaked between 3.55 at 10 mm and 3.88 at 2 mm, reinforcing the dominance to tighter gap spacing in sustaining circulation and delaying flow separation.

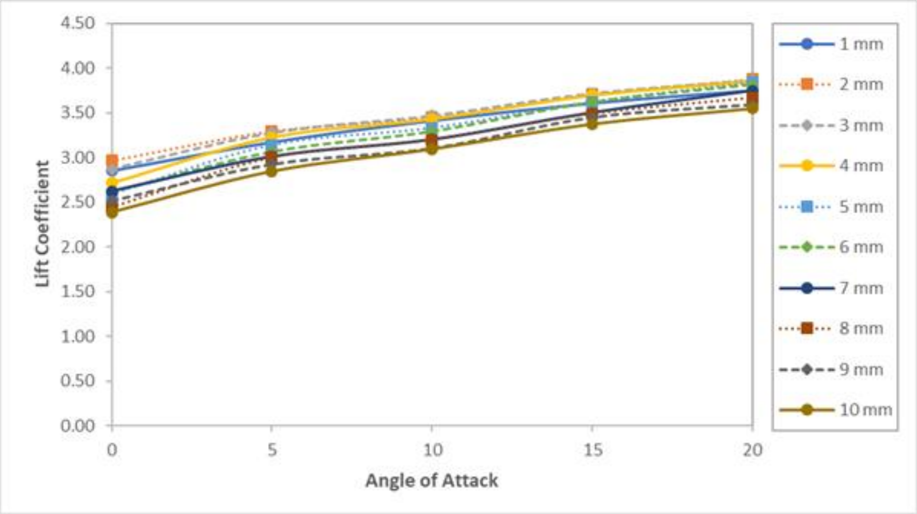

Figure 9: Lift coefficient versus angle of attack for different gap variations at 5 m/s

The C_L difference across gap sizes at 20 degrees was approximately 0.33, which is significant given the relatively low inflow velocity. Interestingly, progression of C_L with angle of attack remained smooth across all gaps, with no evident deterioration in lift even at higher incidence angles. This suggests that at low Reynolds number, the gap effect plays a stabilizing role, particularly for smaller separations, as the CyFlaP system benefits from enhanced interaction of the boundary layers. Overall, the 5 m/s results indicate that narrow gaps, especially between 2 mm and 3 mm, give the most favorable lift performance, offering nearly 9% improvement in C_L compared to wider separations. The improvement arises because tighter gaps enhance the interaction between boundary layers on the adjacent surfaces, strengthening circulation and delaying flow separation. Physically, smaller gaps constrain the flow between the rotating cylinder and the flat plate, increases the shear and accelerates the gap-flow generated by the cylinder's surface motion. This accelerated near-wall flow will increase the local velocity over the leading edge, deepening the suction peak and thereby enhancing the circulation, consistent with the Kutta-Joukowski relation [35]. A reduced gap also limits the cross-flow entrainment and helps maintain a more coherent attached boundary layer, delaying separation and improving the effective turning of the flow around the plate. Prior studies, including Abdulla and Hasan [12], have reported that the optimum lift occurs at intermediate gap sizes because larger gaps weaken the cylinder-induced momentum transfer while excessively small gaps can inhibit flow entrainment or cause adverse pressure buildup. Consequently, C_L peaks at smaller gaps such as 2 mm to 3 mm, where the coupling between the rotating cylinder and the plate is strongest, maximizing the momentum transfer and producing the most favorable pressure distribution for lift generation. As a result, the system sustains higher lift even at larger angles of attack, highlighting the critical role of gap spacing in optimizing the aerodynamic performance at low Reynolds numbers.

At the free-stream velocity of 10 m/s, corresponding to a Reynolds number of 912,279, the gap-dependent trends in lift coefficient became more distinct compared to that of the 5 m/s case as shown in Figure 10. At zero degree, the 1 mm gap recorded a C_L of 2.13, slightly lower than the 2.86 achieved at 5 m/s, suggesting that higher velocities reduced the baseline lift across all gaps. Nonetheless, the narrow gaps maintained a relative advantage, with C_L gradually increasing with angle of attack to reach 2.79 at 20 degrees for the 1 mm case. In contrast, the wider 10 mm gap yielded lower lift levels, from 1.29 at zero degree to 2.51 at 20 degrees, highlighting a widening disparity between narrow and wide spacing as Reynolds number increased. Unlike the smoother progression seen at 5 m/s, the lift response here began to show signs of sensitivity to angle of attack, particularly at intermediate gaps such as 4 mm and 5 mm, where C_L values increased steadily up to 20 degrees without a clear plateau or dip. This indicates that, at 10 m/s, flow attachment near the cylinder to flat plate interface was less stable, with separation effects more evident for mid- to wide-gap configurations. Taken together, the results show that although the general hierarchy of performance for the narrow gaps outperforming wider ones while remains intact, the degree of lift augmentation diminishes compared to the lower velocity conditions, marking an early shift toward Reynolds-number-driven flow dynamics.

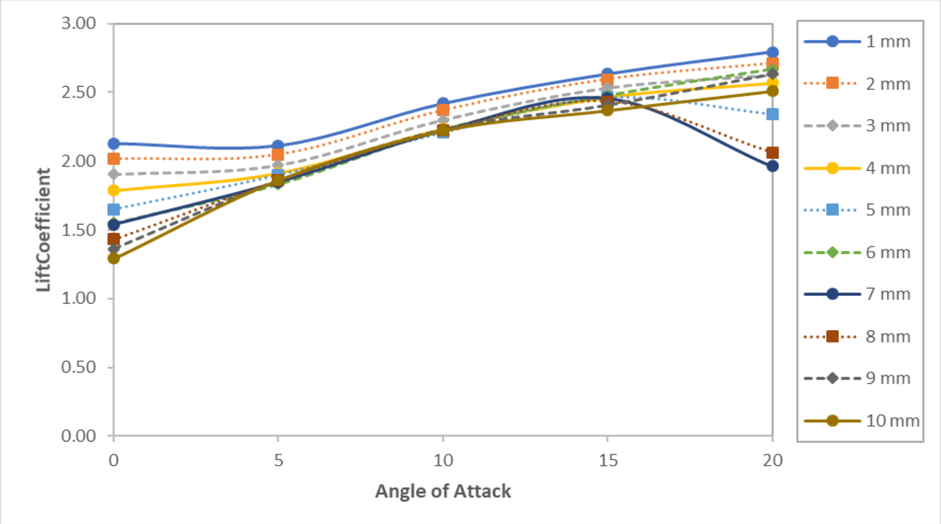

Figure 10: Lift coefficient versus angle of attack for different gap variations at 10 m/s

At 15 m/s, corresponding to Reynolds number of 1,368,419, the relationship between gap spacing and lift coefficient became increasingly nuanced. For 1 mm gap, the C_L initiated at 1.67 at zero degree and climbed steadily to 3.15 at 20 degrees. While still higher than wider-gap configurations, these values were notably lower than those recorded at 10 m/s, confirming that lift generation efficiency weakens as velocity and Reynolds number increase. Wider gaps continued to trail behind for the 10 mm spacing, producing a C_L of 0.93 at zero degree to 1.69 at 20 degrees, widening the disparity between narrow and wide configurations. Intermediate gaps such as 5 mm and 6 mm showed more modest gains, reaching only 1.82 and 1.64 respectively at 20 degrees, underscoring their weaker capacity to sustain circulation compared to the narrow gaps. Unlike the smoother growth patterns evident at lower velocities, the 15 m/s results revealed some irregularities in the lift response, particularly among mid-gap cases where the increments diminished beyond 15 degrees and in some cases hinted at minor reductions. This behavior points to earlier onset of the flow separation and weakened vortex interactions in higher-Re conditions, where the stabilizing influence of narrow gaps became more critical. Overall, Figure 11 underscores a transition although narrow gaps still dominate, the relative gains diminish with rising Reynolds number, suggesting that geometric optimization becomes less influential as inertial effects grow stronger.

At free-stream velocity of 20 m/s, which was corresponding to Reynolds number of 1,824,558, the diminishing benefits of gap optimization became more evident. For 1 mm gap, the C_L started at 1.33 at zero degree and increased steadily to 2.87 at 20 degrees. Although this remained as the highest among all gaps, the improvement beyond 15 degrees was modest compared to lower velocities, reflecting the growing influence of the inertial effects. Wider gaps continued to lag behind, for instance, the 10 mm spacing produced only 0.77 at zero degree and 1.43 at 20 degrees, widening the disparity between the narrow and the wide configurations. Intermediate gaps displayed irregular trends. The 4 mm case, for example, climbed to 1.54 at 10 degrees, dipped slightly to 1.40 at 15 degrees, and then rose sharply to 2.46 at 20 degrees, highlighting unstable flow reattachment dynamics. Unlike smooth and monotonic increases observed at 5 m/s and 10 m/s, the lift curves at this Reynolds number revealed plateaus and abrupt fluctuations, which were characteristic of stronger separation effects. Overall, while narrow gaps still dominate in performance, the relative advantage as shown in Figure 12 diminishes at this higher velocity, signaling a transition toward Reynolds-number-driven flow behavior.

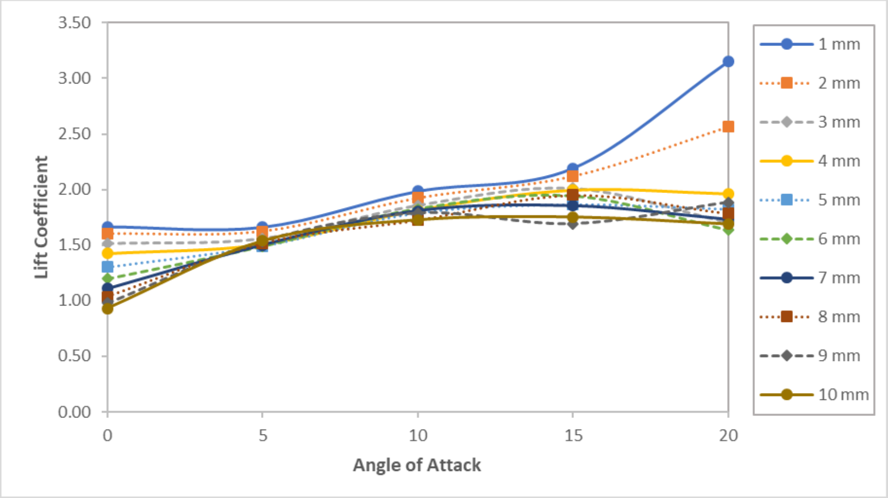

Figure 11: Lift coefficient versus angle of attack for different gap variations at 15 m/s

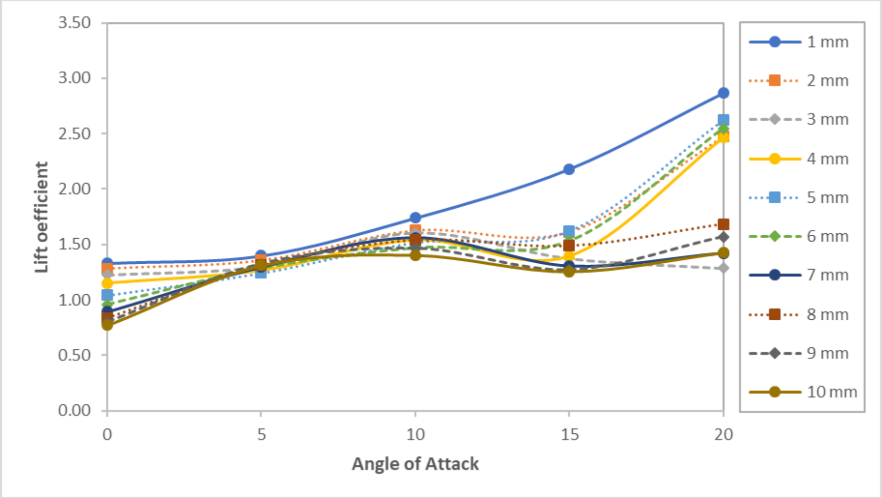

Figure 12: Lift coefficient versus angle of attack for different gap variations at 20 m/s

At 25 m/s, with Reynolds number of 2,280,698, the overall lift levels further continued to decline, underscoring the weakening effect of gap tuning at higher flow speeds. The narrow 1 mm gap, once clearly dominant, produced only 1.40 at 20 degrees, a sharp drop from 2.87 at the same angle in the 20 m/s case. Wider gaps converged toward similarly modest values, with the 10 mm gap delivering 1.24 at 20 degrees. The mid-gap configurations showed more erratic behavior with the 5 mm case climbed gradually to 1.52 at 15 degrees before jumping unexpectedly to 2.62 at 20 degrees, while the 4 mm gap followed a similar surge, reaching 2.07 at 20 degrees. These late peaks suggest that separation-induced reattachment becomes highly unsteady at this velocity, occasionally boosting lift but in an unpredictable fashion. Therefore, the trend at 25 m/s as shown in Figure 13 is one of signals that stability rather than peak lift may be the more relevant metric at this regime.

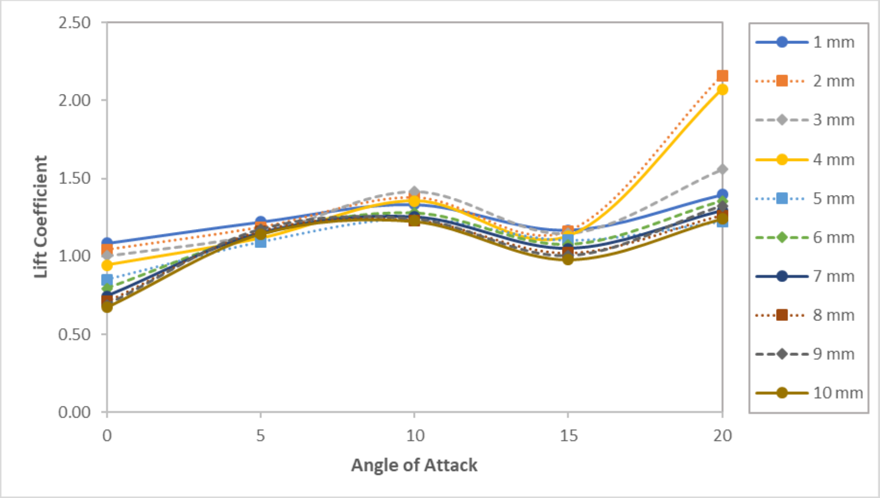

Figure 13: Lift coefficient versus angle of attack for different gap variations at 25 m/s

At 30 m/s, corresponding to Reynolds number of 2,736,838, the lift curves had flattened almost completely, showing that the inertial dominance largely overwhelms the gap-related effects. Across all configurations, C_L values clustered tightly between 0.8 and 1.4 at zero incidence and rarely exceeded 1.37 at 20 degrees as shown in Figure 14. The 1 mm gap, though still nominally ahead with a peak of 1.28 at 20 degrees, no longer exhibited the clear superiority seen at lower speeds. Mid-gap spacing such as 5 mm and 6 mm hovered around 1.35 at best while the widest 10 mm gap barely reached 1.06 at 20 degrees. The uniformity of these outcomes suggests that the system has entered a separation-dominated state in which the boundary-layer interactions contribute little to lift augmentation. In this regime, the optimization of narrow gaps provides only marginal benefits, and the performance hierarchy collapses into a narrow band of diminished effectiveness.

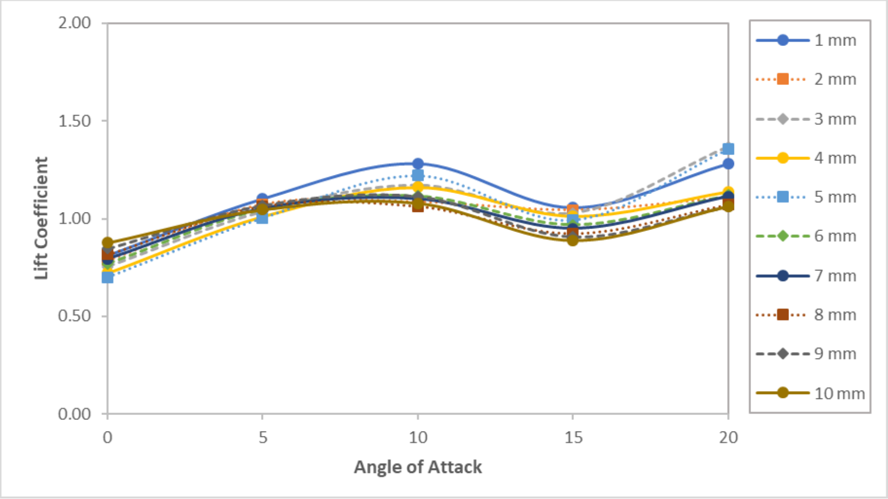

Figure 14: Lift coefficient versus angle of attack for different gap variations at 30 m/s

Across all examined velocities from 5 to 30 m/s, the results demonstrate that gap spacing exerts its strongest influence at low Reynolds numbers where the narrow separations between 1 mm to 2 mm consistently produced the highest C_L, exceeding 3.7 at 20 degrees in 5 m/s case. As velocity increased, the advantage of the small gaps diminished steadily, with intermediate configurations showing irregular patterns and wide gaps offering consistently weaker performance. By 25 m/s and 30 m/s, the lift values had collapsed into a narrow range regardless of the spacing, confirming that the inertial and separation-dominated flow mechanisms ultimately suppress the benefits of the geometric optimizations. Taken together, the findings establish that the gap tuning is most effective in the low to moderate Reynolds number regimes while at higher flow speeds, its influence becomes marginal.

4. Conclusion

This study has examined the aerodynamic performance of the CyFlaP system across a range of gap spacing and free-stream velocities, with emphasis on the lift enhancement achievable through geometric tuning. The results have shown that at low velocities of 5 m/s to 10 m/s, corresponding to Reynolds numbers below one million, narrow gaps of 1 mm to 2 mm delivered the most favorable performance, achieving C_L in excess of 3.7 at 20 degrees. These conditions demonstrated stable lift growth with angle of attack and confirmed that close interaction between the cylinder and the flat plate promotes a strong circulation and delayed separation. As the velocity increased toward 15 m/s and 20 m/s, the absolute lift levels declined and irregularities emerged for intermediate gaps, reflecting earlier onset of separation and weakening of vortex interactions. Wider gaps of 8 mm to 10 mm consistently produced inferior performance, often yielding C_L below 1.5 at higher angles. At highest velocities of 25 m/s and 30 m/s, the overall lift performance converged across all gap sizes, with the values of C_L rarely exceeding 1.4, underscoring the dominance of inertial effects and the diminishing role of geometry in shaping flow behavior. Although the 1 mm gap was identified as the optimal configuration throughout, its practical implementation may be limited by manufacturing tolerances and operational constraints. As such, gaps of 2 mm to 3 mm present a more realistic compromise, offering substantial lift enhancement while maintaining greater feasibility in design and application. Future work may extend this analysis to include unsteady flow effects, structural considerations and three-dimensional configurations to further assess the aerodynamic potential of the CyFlaP concept.

Acknowledgement

This work was supported by the Malaysian Ministry of Education under Fundamental Research Grant Scheme (FRGS/1/2018/TK09/UPM/02/2). The author would also like to thank the Faculty of Engineering, Universiti Putra Malaysia for providing the computational facilities.

References

[1] J. Svorcan, J. M. Wang and K. P. Griffin, ‘Current State and Future Trends in Boundary Layer Control on Lifting Surfaces’, Advances in Mechanical Engineering, vol. 14, no. 7, 2022.

[2] M. Simons, Model Aircraft Aerodynamics. Fox Chapel Publishing, 2025.

[3] S. Abdolahipour, ‘Review on Flow Separation Control: Effects of Excitation Frequency and Momentum Coefficient’, Frontiers in Mechanical Engineering, vol. 10, p. 1380675, 2024.

[4] M. H. Al Faruq, S. I. Pranto, M. Kasfia, J. H. Samin, M. F. Chhoa, A. S. Jahin and H. I. Nokib. (2024). Exploring Magnus Effect: A Review of Its Influence on Airfoil Performance and Industrial Applications [Online]. Retrieved from https://doi.org/10.2139/ssrn.4935291

[5] E. Wolff. (1925). Preliminary Investigation of the Effect of a Rotating Cylinder in a Wing [Online]. Retrieved from https://digital.library.unt.edu/ark:/67531/metadc59069/

[6] E. Wolff and C. Koning. (1926). Tests for Determining the Effect of a Rotating Cylinder Fitted into the Leading Edge of an Airplane Wing [Online]. Retrieved from https://digital.library.unt.edu/ark:/67531/metadc65163/

[7] S. Ahmed, A. Nazari and E. Wahba, ‘Numerical Analysis of Separation Control Over an Airfoil Section’, International Review of Aerospace Engineering, vol. 7, no. 2, pp. 61-68, 2014.

[8] M. N. Huda, T. Ahmed, S. S. Ahmed and M. A. Salam, 'Study of NACA 0010 Symmetric Airfoil with Leading Edge Rotating Cylinder in a Subsonic Wind Tunnel', Proceedings of the 11th International Conference on Mechanical Engineering, Dhaka, Bangladesh, December 2015.

[9] H. M. Ali, A. S. M. Rafie, S. A. M. Ali and E. Gires, 'Computational Analysis of the Rotating Cylinder Embedment onto Flat Plate', CFD Letters, vol. 13, no. 12, pp. 133-149, 2021.

[10] H. M. Ali, A. S. M. Rafie, M. Hamid and S. Ali, 'Comparative Computational Study of Double Rotating Cylinder Embedded on Selig S1223 Aerofoil and Flat Plate for High Altitude Platform', Pertanika Journal of Science and Technology, vol. 30, pp. 2767-2788, 2022.

[11] S. W. Azman, A. S. M. Rafie and E. Gires, 'Aerodynamic Analysis of Cylinder to Flat Plate (CyFlap) Embedment for Agriculture Purposes', Journal of Aeronautics, Astronautics and Aviation, vol. 56, no. 1S, pp. 357-364, 2024.

[12] N. N. Abdulla and M. F. Hasan, 'Effect of Gap between Airfoil and Embedded Rotating Cylinder on the Airfoil Aerodynamic Performance', Research & Development in Material Science, vol. 3, no. 4, 2018.

[13] F. Z. Wang, I. Animasaun, T. Muhammad and S. Okoya, 'Recent Advancements in Fluid Dynamics: Drag Reduction, Lift Generation, Computational Fluid Dynamics, Turbulence Modelling and Multiphase Flow', Arabian Journal for Science and Engineering, vol. 49, no. 8, pp. 10237-10249, 2024.

[14] M. I. Kamid, H. M. Ali and A. S. M. Rafie, 'Computational Aerodynamics Analysis of a Bluff Body with Rotating Cylinder as Drag Reducer', Journal of Aerospace Society Malaysia, vol. 1, no. 1, pp. 34-45, 2023.

[15] M. S. I. Roslan, H. M. Ali and A. S. M. Rafie, 'Rotational Speed Analysis on Double Rotating Cylinder for Cylinder to Flat Plate using Numerical Method', Journal of Aeronautics, Astronautics and Aviation, vol. 55, no. 3S, pp. 495-506, 2023.

[16] U. Z. Zaimi, H. M. Ali and A. S. M. Rafie, 'Experimental Analysis on Pitching Moment for Embedment Cylinder to Flat Plate High Altitude Platform Station', in International Seminar on Aeronautics and Energy, Springer, 2022.

[17] M. A. Akar and H. Akıllı, 'Base Bleed Flow Control Tool for Circular Cylinders with Three Side-By-Side Arrangements in Shallow Water', International Journal of Pioneering Technology and Engineering, vol. 2, no. 01, pp. 128-134, 2023.

[18] H. M. Ali, A. S. M. Rafie, M. F. A. Hamid and S. A. M. Ali, 'Concentrated Flow Effects on Aerodynamics Performance for CyFlaP Magnus UAV by using Computational Approach', CFD Letters, vol. 18, no. 3, pp. 134-151, 2025.

[19] J. Liu, W. Ma, D. Zheng, L. Jin and Q. Liu, 'Numerical Investigation of Cylinder Rotors with Various Endplates', Physics of Fluids, vol. 36, no. 7, 2024.

[20] H. Zhu, T. Tang, M. M. Alam, J. Song and T. Zhou, 'Flow-induced Rotation of a Circular Cylinder with a Detached Splitter Plate and Its Bifurcation Behavior', Applied Ocean Research, vol. 122, p. 103150, 2022.

[21] Y. Zhang and Y. Zhao, 'Novel Design of a Circulation Control Airfoil with Cylinder Rotation', Physics of Fluids, vol. 35, no. 8, 2023.

[22] A. Boral, S. Dutta, A. Das, A. Kumar, N. Bej, P. Chaubdar, B. N. Das and A. B. Harichandan, 'Drag Reduction for Flow Past Circular Cylinder using Static Extended Trailing Edge', ASME Open Journal of Engineering, vol. 2, p. 021016, 2023.

[23] K. Subramaniam and W. S.-I. W. Salim, 'A Review of Experimental Approaches for Investigating the Aerodynamic Performance of Drones and Multicopters', Journal of Advanced Research in Experimental Fluid Mechanics and Heat Transfer, vol. 14, no. 1, pp. 1-24, 2023.

[24] C. Badalamenti and S. Prince, 'Effects of Endplates on a Rotating Cylinder in Crossflow', Proceedings of 26th AIAA Applied Aerodynamics Conference, Honolulu, USA, August 2008.

[25] A. Betz, ‘Der magnuseffekt, die grundlage der flettner—walze’, Zeitschrift des vereins deutscher Ingenieure. Translated to: The “Magnus Effect” The Principle of the Flettner Rotor. NACA Technical Memorandum, TM-310, pp. 9-14, 1925.

[26] E. Barati, M. R. Zarkak and J. A. Esfahani, ‘Effect of Rotational Direction of Circular Cylinder for Mixed Convection at Subcritical Reynolds Number’, Proceedings of the 27th Annual International Conference of Iranian Society of Mechanical Engineers, Tehran, Iran, April-May 2019.

[27] S. Wang, X. Zhang, G. He and T. Liu, ‘A Lift Formula Applied to Low-Reynolds-Number Unsteady Flows’, Physics of Fluids, vol. 25, no. 9, 2013.

[28] G. E. Torres and T. Mueller, ‘Aerodynamic Characteristics of Low Aspect Ratio Wings at Low Reynolds Numbers’, Progress in Astronautics and Aeronautics, vol. 195, pp. 115-141, 2001.

[29] V. Modi, ‘Moving Surface Boundary-Layer Control: A Review’, Journal of Fluids and Structures, vol. 11, no. 6, pp. 627-663, 1997.

[30] H. M. Ali, A. S. M. Rafie and S. A. M. Ali, ‘Numerical Analysis of Leading Edge Cylinder Aerofoil on Selig S1223 for Moving Surface Boundary Control’," Journal of Aeronautics, Astronautics and Aviation, vol. 53, no. 2, pp. 143-153, 2021.

[31] A. Mgaidi, A. Rafie, K. Ahmad, R. Zahari, M. A. Hamid and O. Marzuki, ‘Numerical and Experimental Analyses of the Flow Around a Rotating Circular Cylinder at Subcritical Regime of Reynolds Number using k-ε and k-ω-sst Turbulent Models’, ARPN Journal of Engineering and Applied Sciences, vol. 13, no. 3, pp. 954-960, 2018.

[32] F. R. Menter, ‘Two-equation Eddy-viscosity Turbulence Models for Engineering Applications’, AIAA Journal, vol. 32, no. 8, pp. 1598-1605, 1994.

[33] D. C. Wilcox, ‘Reassessment of the Scale-Determining Equation for Advanced Turbulence Models’, AIAA Journal, vol. 26, no. 11, pp. 1299-1310, 1988.

[34] Q. Yao, C. Zhou and C. Wang, ‘Numerical Study of the Flow Past a Rotating Cylinder at Supercritical Reynolds Number’, Proceedings of 4th International Conference on Mechanical Materials and Manufacturing Engineering, Wuhan, China, October 2016.

[35] J. Anderson, Fundamentals of Aerodynamics. McGraw Hill, 2011.

JOURNAL OF AEROSPACE SOCIETY MALAYSIA

FLEXIBLE WING DESIGN STRUCTURAL PERFORMANCE UNDER STATIC AEROELASTIC CONDITION

Nur Namierah Abdul Aziz[1], Mohammad Yazdi Harmin[1] and Hidayatullah Mohammad Ali[1, *]

1. Department of Aerospace Engineering, Faculty of Engineering, Universiti Putra Malaysia, 43400 Serdang, Selangor, Malaysia

*Correspondence: hidayatullah@upm.edu.my

Abstract: This study investigates the static aeroelastic response of a flexible wing, emphasizing the role of the internal rib configurations in governing the structural deflection and stiffness. With the aerospace industry advancing toward lighter weight, having high-aspect-ratio wings and achieving the structural efficiency without compromising integrity has become a central design challenge. A baseline aluminum wing box was developed using finite element methods, fabricated and experimentally validated through experimental modal analysis (EMA). To improve model accuracy, design sensitivity and optimization (SOL 200) was employed to refine material properties, ensuring close validation between simulated and measured natural frequencies. Using the validated model, multiple rib configurations were evaluated under aerodynamic loading via the linear static analysis (SOL 101) at a fixed angle of attack. The results demonstrate that rib topology strongly influences static aeroelastic behavior. In particular, optimized rib layouts reduced the wingtip deflection and also improved the natural frequencies by up to 13%, indicating enhanced stiffness without added weight. On the whole, findings from this study highlights the potential of rib configuration tailoring as an effective aeroelastic strategy for lightweight aircraft and unmanned aerial systems, advancing the structural optimization practices through the integration of simulation, experimental validation and fabrication.

Keywords: aeroelastic tailoring, aeroelasticity, finite element analysis, flexible wing, rib configuration

1. Introduction

The pursuit of improved aerodynamic efficiency in modern aircraft has driven the adoption of the slender, high–aspect ratio wing (HARW) designs [1]. Although they are aerodynamically advantageous, such configurations also exhibit greater structural flexibility [2], making them susceptible to aeroelastic instabilities such as torsional divergence, large deflections and control surface reversion [3]. Aeroelastic tailoring of the wing, particularly through the rib configuration, has emerged as a promising strategy to enhance stiffness while avoiding significant weight penalties [4].

Aeroelasticity is broadly categorized into static and dynamic phenomena. Static aeroelastic effects include divergence and control reversal whereas dynamic aeroelasticity relates to flutter and limit cycle oscillations [3]. While dynamic aeroelastic instabilities, especially flutter, have been widely studied due to their catastrophic consequences, the static domain has received comparatively less attention despite its strong influence on the wing deflection and load distribution. Prior work has shown that tailoring the internal wing structures can significantly affect aeroelastic response. Patil and Hodges [2] highlighted the importance of geometric nonlinearities in HARWs while Ting et al. [5] applied the finite-element vortex-lattice method to model static aeroelasticity. Krüger et al. [6] further demonstrated that structural tailoring can alleviate aerodynamic loads in demonstrator wings. The rib and spar configurations play a central role in the tailoring strategies [7]. Stanford [8] introduced bi-level optimization method to refine rib placement, sizing and wing shaping, showing that curved or unconstrained rib arrangements could improve load path efficiency and expand the aeroelastic design space. Othman et al. [4] investigated rib orientations in a rectangular wing box, resulting in the increment of torsional frequency up to 8.5% and flutter speed gains up to 80% as compared to conventional designs. Robinson et al. [9] extended these findings by employing the SpaRib concepts with curvilinear spars and ribs, achieving improved bend–twist coupling and delayed flutter without mass penalties. Locatelli et al. also showed that incorporating curvilinear spars and ribs (SpaRibs) into the wing structures can substantially enhance their structural performance [10]. Related studies have also explored topology optimization of rib–spar layouts [2], rib thickness variations [11] and experimental assessments of the unconventional rib configurations [4, 10], collectively reinforcing the centrality of rib management in aeroelastic tailoring.

Despite these advances, much of the literatures emphasizes flutter or dynamic phenomena, leaving static aeroelastic behavior comparatively underexplored. This gap is critical as static deflection directly affects aerodynamic efficiency, load transfer and structural integrity [2]. To address this, the present study investigates the static aeroelastic response of a flexible aluminum wing with unconventional rib configurations. A validated baseline wing model, established through the experimental modal analysis, serves as the reference for comparison. Building on this foundation, the research evaluates how the rib spacing and the rib count influence both deflection and stiffness under steady aerodynamic loading. By correlating experimental and numerical findings, the study quantifies how rib management can improve the stiffness without any added structural mass. The outcomes provide both fundamental insight into aeroelastic tailoring and practical guidance for lightweight aircraft and unmanned aerial vehicle (UAV). Overall, this work contributes to the aeroelastic tailoring research by shifting the emphasis toward static aeroelastic effects and validating unconventional rib configurations stiffness. The results provide new evidence that the rib spacing and distribution can mitigate deflection, improve stiffness and support the development of efficient high–aspect ratio wing designs.

2. Methodology

This study was conducted in three main phases. Firstly, a baseline wing model was developed and numerically analyzed to establish the reference performance. Secondly, the model was fabricated and validated through the experimental testing to ensure consistency between the physical and numerical models. Finally, static aeroelastic analyses were performed to evaluate the effects of the alternative rib configurations on wing stiffness and deflection. All computational analyses were carried out using MSC Nastran [12], employing the following Solution Sequences (SOL):

(a) SOL 103 (Normal Mode Analysis): to extract natural frequencies and mode shapes
(b) SOL 101 (Linear Static Analysis): to evaluate deflections under aerodynamic loading
(c) SOL 145 (Flutter Analysis): to determine flutter onset speeds
(d) SOL 200 (Design Sensitivity and Optimization): to refine material properties for improved correlation with experimental data

2.1 Structural model

The baseline wing was modeled as a half-wing configuration with an aspect ratio (AR) of 7, two C-shaped spars and eight C-shaped ribs. The structure was modeled in aluminum, which was chosen for its high strength-to-weight ratio and ease of fabrication. The material was assumed homogeneous and isotropic, with Young's modulus of 70 GPa, Poisson's ratio value of 0.35 and density with 2700 kg/m^3. Meshing seed was applied at the model curves and equivalencing the mesh using tolerance cube method with 0.005 equivalencing tolerance. The spars had dimensions of 0.01 m width, 0.015 m height and 0.001 m thickness while the ribs were measured 0.01 m width, 0.013 m height and 0.001 m thickness. A boundary condition was applied at the wing root, ensuring no rotational or translational movement in the x, y and z axis at the root. Aerodynamic loading was determined using the thin airfoil theory, expressed as Equation 1, where L is lift force, ϱ is air density with a constant value of 1.225 kg/m³, V is freestream velocity of 5 m/s to 25 m/s, S is wing strip area and C_L is lift coefficient at angles of attack (AOA) of 2° and 10°.

$$L = \frac{1}{2}\rho V^2 S C_L \tag{1}$$

The loads were distributed along the front spar using the strip method as indicated in Figure 1. A Linear Static Analysis (SOL 101) was conducted to assess the deflections under aerodynamic loading, with the maximum deflection constrained to 0.3 m based on the wind tunnel limitations. Flutter analysis (SOL 145) was also performed to confirm flutter onset within 20 m/s to 25 m/s. If these conditions were not met, the span and chord dimensions were adjusted, and the process was repeated. The finalized configuration, which satisfied both structural and also aeroelastic criteria, was established as the baseline wing model.

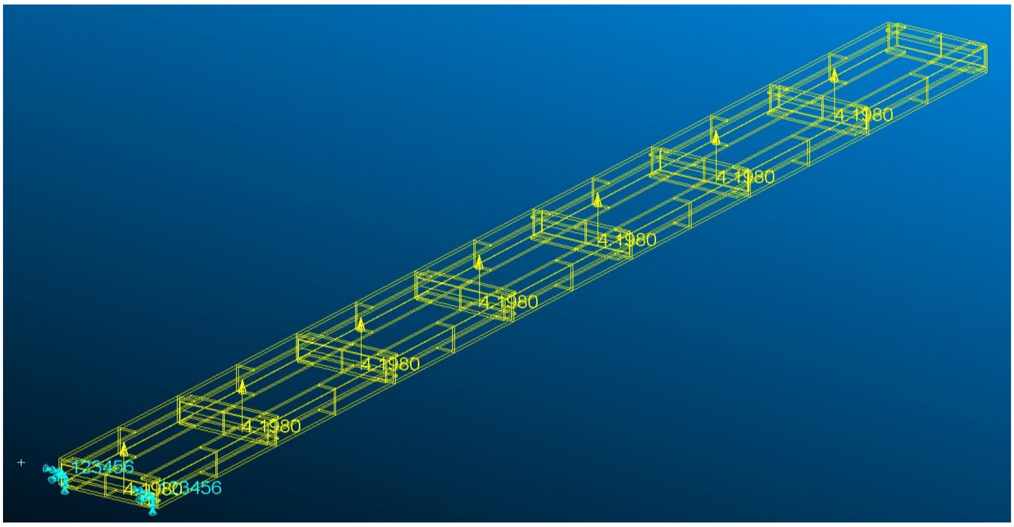

Figure 1: Loads applied on front spar

2.2 Fabrication and experimental validation

The baseline wing box was fabricated using T6 aluminum sheets of 0.001 m thickness. Metal sheets were cut to dimension using a cut-off machine, bent into C-shaped profiles and assembled with rivets following the detailed CAD drawings and assembly guides. A 4-cm spar extension was included for the clamping purposes. The completed wing box was covered with a curved styrofoam surface to represent the aerodynamic profile.

A custom clamp was designed using CAD and 3D-printed in PLA with 80% infill density to secure the wing root during testing. This ensured the boundary conditions were consistent with the FE model. The fabricated wing box underwent experimental modal analysis (EMA) using roving impact hammer test as displayed in Figure 2. Accelerometers were mounted spanwise and impact excitation was applied at multiple points. The frequency response functions (FRFs) were recorded, which were then processed to extract natural frequencies and mode shapes. These were compared with FEA results to validate the baseline model.

Figure 2: Experimental modal analysis (EMA) setup

Upon validation, SOL 200 iteratively adjusts the Young's Modulus, Poisson's ratio and also density. This solution sequence performs design sensitivity analysis and automated optimization to identify the most suitable material property set, in which the boundary range applied is the properties current values. The solver then iteratively adjusts these variables, whereby the optimized values are then applied in the model and the Normal Mode Analysis (SOL 103) is performed. The revised natural frequencies are extracted and compared against both the original simulation results and the experimental data to verify improvement. The optimized material properties are subsequently applied in the following stages of the project, including the static analysis of modified rib configurations.

2.3 Rib configuration analysis

Two categories of rib modifications were examined in this study, which included non-uniform rib spacing and rib count variation. For non-uniform spacing, two models with eight ribs were developed, one with increasing spacing from 6 cm at the root to 18 cm at the tip as depicted in Figure 3a, and one with decreasing spacing from 18 cm at the root to 6 cm at the tip as in Figure 3b. Two additional configurations were created with 10 ribs as presented in Figure 4a and 12 ribs in Figure 4b, uniformly spaced across the span. Loads identical to the baseline model were applied using the strip theory at 10° AOA and velocities of 5, 10, 15, 20 and 25 m/s. A Linear Static Analysis (SOL 101) was conducted to evaluate deflection responses.

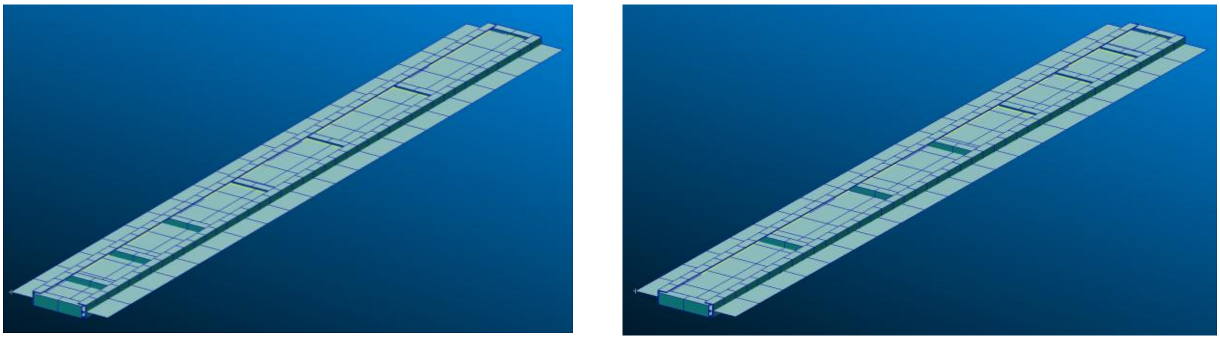

(a) Increasing spacing

(b) Decreasing spacing

Figure 3: Models with varying spacing

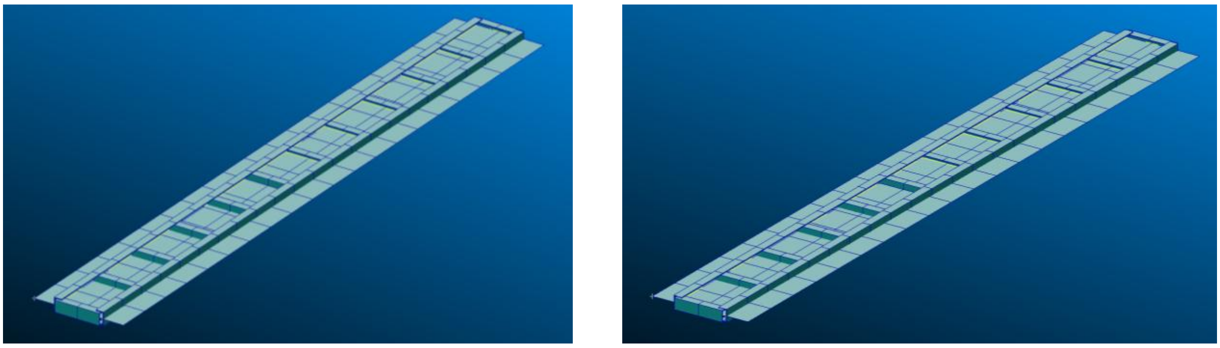
(a) 10 ribs (b) 12 ribs

Figure 4: Models with varying ribs number

The configuration yielding the lowest deflection was further analyzed using Normal Mode Analysis (SOL 103) to extract natural frequencies and mode shapes. The percentage differences relative to the baseline were calculated to evaluate stiffness improvements. The configuration with the best combined performance in static and modal analyses was selected as the optimal rib arrangement for this study.

3. Results and Discussion

The results are organized into three parts: baseline wing development, experimental validation and analysis of the unconventional rib configurations. Numerical and experimental findings are integrated to demonstrate how the rib layout influences the wing deflection and stiffness under static aeroelastic conditions.

3.1 Baseline design development

Five half-wing designs, each with an aspect ratio of seven and eight ribs, were initially evaluated to identify the suitable baseline configuration. The selection was guided by two performance constraints: a maximum wingtip deflection of 0.3 m and a flutter onset speed not exceeding 25 m/s, consistent with the dimensional and operational limitations of the closed-loop wind tunnel test section of 1 m × 1 m × 3 m. Each design was subjected to Linear Static Analysis (SOL 101) at the angles of attack (AOA) of 2° and 10°. The translational deflections were found to be consistently lower and also very minimal than rotational deflections. Given the negligible effect, it can be omitted in this discussion for clarity and simplicity. Among the designs, the half wing with span 0.63 m and chord length of 0.09 m had demonstrated the lowest deflection of 0.03 m while the half wing with span 0.84 m and chord length of 0.12 m exhibited the highest, reaching 0.28 m at 10° AOA and 25 m/s. Despite this, all designs remained within the allowable limit. Nevertheless, the trend confirmed that increasing span leads to higher deflections due to reduced stiffness.

Flutter performance was assessed using SOL 145, only half wing with span of 0.84 m and chord length of 0.12 m satisfied the flutter constraint, with onset occurring at 21.3 m/s. This result indicated that while longer spans increased deflection, they also shifted flutter onset to higher speeds, reflecting increased structural rigidity. Based on compliance with both criteria, the half wing with span of 0.84 m and chord length of 0.12 m was selected as the baseline model. A Normal Mode Analysis (SOL 103) was subsequently performed to extract the natural frequencies and mode shapes.

3.2 Baseline model validation

The fabricated baseline wing box was validated experimentally through experimental EMA using the roving impact hammer test. The resulting FRFs enabled extraction of natural frequencies and mode shapes. A comparison between simulated and experimental frequencies is presented in Table 1.

Table 1: Frequencies from EMA and FEA

Mode	EMA Natural Frequency (Hz)	FEA Natural Frequency (Hz)	Percentage Error (%)
1	14.6722	20.9699	42.92
2	38.5121	33.8300	12.16
3	110.0344	130.3570	18.47
4	157.2872	157.4560	0.11
5	312.8636	361.0750	15.41
6	385.5028	407.1590	5.62

Comparisons between the simulated and the experimental natural frequencies showed significant deviations in bending modes. Mode 1 exhibited a 42.92% error while Mode 3 and Mode 5 deviated by 18.47% and 15.41%, respectively. Torsional modes from Modes 2, 4 and 6 displayed smaller percentage errors, suggesting that the torsional stiffness was better captured in the simulation. The percentage error may be attributed to the fabrication imperfections from the model fabrication material offset, which is the Aluminum 6061-T6, and also the experimental variations such as model experimental orientation and the styrofoam on the spars acting as a damper, which lowers the measured natural frequency.

To improve the validation, Design Sensitivity and Optimization Analysis (SOL 200) was conducted by adjusting Young's modulus, Poisson's ratio and density within defined bounds to refine the model properties. The updated properties are optimized at Young's Modulus of 6.0138×10^{10}, Poisson ratio of 0.05233 and density of 3106.9895 kg/m^3, which were then applied to the baseline model and updated frequencies were obtained as presented in Table 2. Although the optimized Poisson's ratio differs from standard aluminum values of 0.3 [12], its use in this study is strictly limited to improving the correlation between the FEA and the EMA.

Table 2: Frequencies from EMA and updated baseline FEA

Mode	EMA Natural Frequency (Hz)	FEA Natural Frequency (Hz)	Percentage Error (%)
1	14.6722	18.19	23.98
2	38.5121	30.43	20.99
3	110.0344	113.16	2.84
4	157.2872	138.53	11.93
5	312.8636	313.79	0.30
6	385.5028	355.49	7.79

The updated model showed improved correlation in the bending modes while torsional frequencies deviated slightly more, suggesting an enhanced flexural stiffness but reduced torsional stiffness. On average, the percentage error decreased to approximately 23%. Despite remaining discrepancies, largely attributed to the fabrication imperfections in Aluminum 6061-T6, minor cracking during forming and damping from the Styrofoam fairings, the experimental results had validated the baseline as sufficiently accurate for further analysis. Importantly, the mode shapes remained consistent across simulations and experiments, confirming structural accuracy.

3.3 Static analysis of unconventional rib configurations

With the validated model established, alternative rib configurations were examined to determine their influence on static performance. Two unconventional designs were first considered, one with rib spacing increasing toward the tip and another with spacing decreasing toward the tip, each with eight ribs. Deflection responses at 10° AOA and across velocities of 5 to 25 m/s are shown in Figure 5**.**

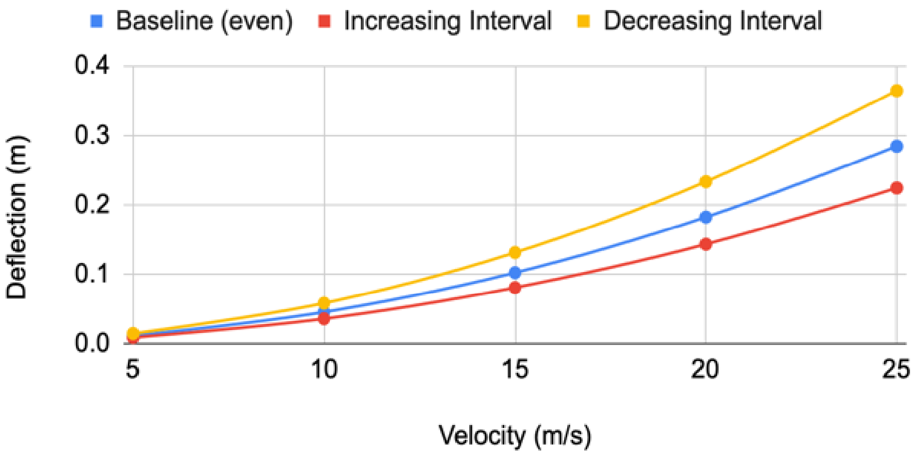

Figure 5: Effect of rib spacing on rotational deflection

The optimized baseline exhibited higher rotational deflections than the original baseline, with the values of 0.288 m at 25 m/s, consistent with reduced stiffness indicated by lower natural frequencies. Among the new configurations, the increasing rib spacing model performed best, recording 0.224 m of deflection at 25 m/s. In contrast, the decreasing spacing design performed worse, with 0.364 m. These results highlighted the role of rib spacing in distributing the load transfer and stiffness, where evenly distributing load paths increases stiffness while clustering the ribs near the root decreases the structural efficiency.

Figure 6 displays the deflection responses for different rib counts with equal spacing. The graph indicates that an increase in the number of ribs corresponds to greater deflection. An increased number of ribs at 10, which is additional of 2 ribs from the baseline, deflects at 0.359 m in rotational deflection at 25 m/s. While for 12 ribs, an addition of 4 ribs to the baseline, also shows an increase on deflection with torsional deflection at 0.426 m. This suggests that a higher rib count reduces the overall stiffness of the structure, which can be attributed to the additional weight introduced by the extra ribs.

Table 3 and Table 4 tabulate the results of the Normal Mode Analysis (SOL 103) on the best rib configuration, which is the increasing spacing. Table 3 shows an average improvement of 13.66% in natural frequencies compared to the baseline, across both bending and torsional modes. Table 4 shows the rotational deflection is reduced by approximately 22% across all modes, demonstrating enhanced torsional rigidity. On the whole, the results validate the increasing-spacing configuration as the optimal rib arrangement, offering enhanced stiffness.

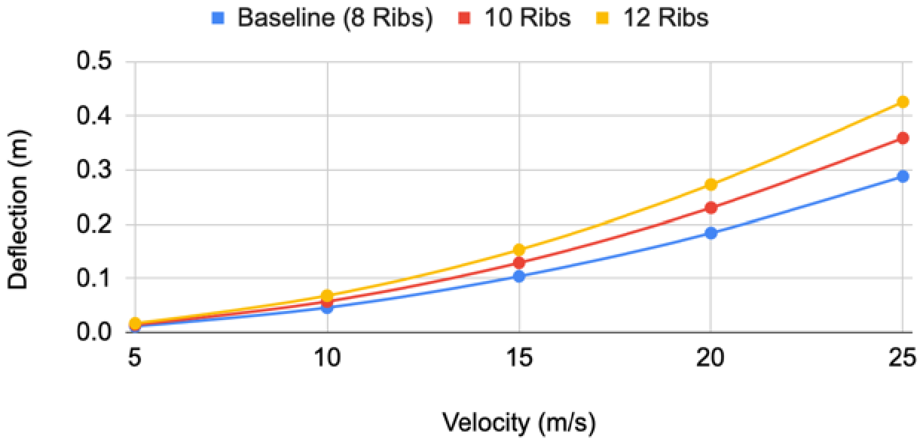

Figure 6: Effect of number of ribs on rotational deflection

Table 3: Comparison of baseline and optimized natural frequency

Mode	Baseline Natural Frequency (Hz)	Optimized Natural Frequency (Hz)	Improvement (%)
1	18.19	21.52	18.31
2	30.43	33.31	9.46
3	113.16	131.59	16.29
4	138.53	154.047	11.20
5	313.79	361.12	15.08
6	355.49	396.83	11.63

Table 4: Comparison of baseline and optimized rotational deflection

Velocity (m/s)	Baseline Deflection (m)	Optimized Deflection (m)	Improvement (%)
5	0.01	0.01	22.17
10	0.05	0.04	22.17
15	0.10	0.08	22.60
20	0.18	0.14	22.28
25	0.29	0.22	22.22

The analyses confirmed that both rib spacing and rib count significantly influence the stiffness and deflection. The study validated the hypothesis that aeroelastic tailoring through the rib management can enhance the structural performance without increasing mass. The results also highlight that increasing rib spacing toward the tip improves stiffness and reduces deflection while increasing rib count reduces stiffness due to the added weight. These findings provide practical guidance for structural optimization of lightweight, high-aspect-ratio wings, reinforcing the importance of rib topology in aeroelastic design.

4. Conclusion

This study investigated the structural performance of the flexible wing under the static aeroelastic conditions, focusing on rib configuration effects. A baseline aluminum wing box with eight C-shaped ribs and two spars was developed using FEA, fabricated and validated through EMA. The experimental natural frequencies and mode shapes showed a good agreement with the simulations, confirming the accuracy of the numerical model. Modified rib layouts demonstrated that rib topology critically affects the structural response, with an average improvement of natural frequency up to 13.66% in comparison with the baseline performance, confirming that rib management enhances structural stability without additional weight, offering a lighter aircraft and improved performance. Moving forward, future work should address dynamic aeroelastic phenomena, explore advanced rib topologies and perform wind tunnel validation for broader application. In conclusion, strategic rib spacing and distribution provide a simple yet effective strategy of improving stiffness and structural efficiency, contributing to more sustainable high-aspect-ratio wing designs.

Acknowledgement

The authors gratefully acknowledge the guidance and encouragement of their supervisors, whose expertise was invaluable to the completion of this work. Appreciation is also extended to all individuals who contributed directly or indirectly to this study. Finally, the authors extend their appreciation to the broader community of researchers and practitioners who will benefit from these findings.

References

[1] Y. Ma, S. Karpuk and A. Elham, 'Conceptual Design and Comparative Study of Strut-Braced Wing and Twin-Fuselage Aircraft Configurations with Ultra-High Aspect Ratio Wings', Aerospace Science and Technology, vol. 121, p. 107395, 2022.

[2] S. Kilimtzidis and V. Kostopoulos, 'Multidisciplinary Structural Optimization of Novel High-Aspect Ratio Composite Aircraft Wings', Structural and Multidisciplinary Optimization, vol. 66, no. 7, 150, 2023.

[3] J. Čečrdle, Whirl Flutter of Turboprop Aircraft Structures. Woodhead Publishing, 2015.

[4] M. Y. Harmin, M. S. Othman, F. I. Romli, 'Parametric Study on the Flutter Characteristics of a Simple Rectangular Wing-Box Model with Varying Ribs Orientation', International Journal of Pure and Applied Mathematics, vol. 119, no. 15, pp. 3771–3777, 2018.

[5] E. Ting, N. T. Nguyen and K. V. Trinh, 'Static Aeroelastic and Longitudinal Trim Model of Flexible Wing Aircraft using Finite-Element Vortex-Lattice Coupled Solution', Proceedings of AIAA/ASME/ASCE/AHS/ASC Structures, Structural Dynamics and Materials Conference, Natural Harbor, USA, January 2014.

[6] W. R. Krüger, Y. M. Meddaikar, J. K. S. Dillinger, J. Sodja and R. De Breuker, 'Application of Aeroelastic Tailoring for Load Alleviation on a Flying Demonstrator Wing', Aerospace, vol. 9, no. 10, p. 535, 2022.

[7] United States Department of Transportation. (2023). FAA-H-8083-31B Aviation Maintenance Technician Handbook – Airframe [Online]. Retrieved from https://www.faa.gov/regulations_policies/handbooks_manuals/aviation/FAA-H-8083-31B_Aviation_Maintenance_Technician_ Handbook.pdf

[8] B. Stanford, 'Shape, Sizing and Topology Design of a Wingbox Under Aeroelastic Constraints', Journal of Aircraft, vol. 58, no. 6, pp. 1406-1415, 2021.

[9] J. H. Robinson, J. T. Allison and R. J. Seethaler, 'Aeroservoelastic Optimization of Wing Structure using Curvilinear Spars and Ribs (SPARIBS)', Proceedings of 12th AIAA/ISSMO Multidisciplinary Analysis and Optimization Conference, Washington DC, USA, June 2016.
[10] L. Meng, J. Zhang, Y. Hou, P. Breitkopf, J. Zhu and W. Zhang, 'Revisiting the Fibonacci Spiral Pattern for Stiffening Rib Design', International Journal of Mechanical Sciences, vol. 246, p. 1081312023, 2023.
[11] R. F. Latif, M. K. A. Khan, A. Javed, S. I. A. Shah and S. T. I. Rizvi, 'A Semi-Analytical Approach for Flutter Analysis of a High-Aspect-Ratio Wing', The Aeronautical Journal, vol. 125, no. 1284, pp. 410–429, 2021.
[12] A. P. Mouritz, Introduction to Aerospace Materials. Woodhead Publishing, 2012.
[13] W. Rodden and E. Johnson, MSC/NASTRAN Aeroelastic Analysis User's Guide. The MacNeal-Schwendler Corporation, 1994.

EXPERIMENTAL PASSIVE FLOW CONTROL ON AHMED MODEL FOR AERODYNAMIC DRAG REDUCTION

Ananta Kullan [1, *], Shabudin Mat [2] and Rafiqi Daniel Ramadhan [2]

1. Faculty of Mechanical Engineering, Universiti Teknologi Malaysia, Malaysia.
2. UTM Aerolab, Institute for Sustainable Transport, Universiti Teknologi Malaysia, Malaysia.

*Correspondence: nanthakva@live.com

Abstract: This study presents an investigation on the effects of yaw and slant angles to the aerodynamic behavior of the Ahmed model. Experiments were conducted in a low-speed wind tunnel at a constant speed of 25 m/s across different yaw angles. Four Ahmed models with slant back angles of 0°, 15°, 25° and 40° were used. All in all, the experimental results indicate that yaw angle significantly influences the aerodynamic behavior of the Ahmed model. As the yaw angle increases, the pressure distribution also becomes increasingly asymmetric due to changes in flow separation and wake formation. Additionally, the findings also highlight the influence of slant angle variations under yawed conditions, an area with limited prior investigation. The obtained knowledge on the aerodynamic behavior of the Ahmed model from this study is very useful in further vehicle design development that is based on this generic model.

Keywords: aerodynamic characteristics; Ahmed model; slant angle; vehicle aerodynamics; wind tunnel

1. Introduction

Aerodynamic drag significantly affects the energy efficiency and also environmental impact of road vehicles. For instance, a 15% reduction in drag can result in up to a 5% improvement in fuel economy, making aerodynamic optimization vital for internal combustion engine vehicles (ICEVs) and electric vehicles (EVs). Among various vehicle body types, bluff-body shapes with blunt rear ends are prone to pressure drag due to flow separation and wake formation. The Ahmed body, introduced by Ahmed et al. in 1984, serves as the benchmark model to study the bluff-body aerodynamics due to its geometric simplicity and also its relevance to the real-world vehicle designs [1]. It has been widely adopted in both experimental and numerical investigations to explore the flow control strategies aimed at reducing drag.

Flow control techniques and methods have been applied to reduce the drag, which are categorized into active and passive methods. In essence, the active flow control methods involve energy input to manipulate the flow field. Techniques such as steady blowing, synthetic jets and the Coanda effect have shown promising results in wake control and drag reduction. For instance, a conducted study reported a 10% reduction in the base drag using Coanda-induced flow deviation, which extended the wake length and reduced its width [2]. In addition, another study has also demonstrated that localized suction and blowing could effectively control the separation bubble and suppress swirling structures at the rear of the Ahmed body [3]. Although highly effective, active methods require precise control and energy input, making them less suitable for mass-market applications. On the other hand, passive flow control devices such as vortex generators (VGs), base cavities, deflector plates and geometric modifications (i.e. roof-edge rounding) offer energy-free methods to delay flow separation and reduce drag. Bayindirli (2024) demonstrated that the roof-mounted VGs could increase surface adherence and reduce pressure drag by disturbing the laminar separation [4]. Additionally, different VG geometries and their aerodynamic effectiveness have been explored [5], which highlights that their application is not merely aesthetic but also functional.

It has been shown that the flow separation at the blunt rear and nose sections is the primary source of drag forces in bluff bodies [6]. Therefore, by modifying the Ahmed body geometry and validating it against experimental data using standard k-turbulence model, this study will contribute valuable insights into the effects of passive devices on complex wake flows. A critical gap in current research is the lack of studies examining the combined influence of yaw angle and rear slant angle on the aerodynamics of Ahmed body. While many investigations isolate the effects of either yaw or slant angle, few studies have considered their interaction. Real-world vehicles often operate under the crosswind (yawed) conditions, which interact with the vehicle's rear geometry to influence separation and wake behavior. This gap has been highlighted by Sumnu and Eraslan (2025), noting that very few studies simultaneously explore the effects of passive control strategies and shape optimization under yawed flow [7]. This oversight limits the generalizability of findings to actual operating conditions of the vehicles.

Although computational fluid dynamics (CFD) studies have advanced significantly, many of them still rely on coarse grids or simplified turbulence models. High-fidelity simulations incorporating fine meshes and advanced turbulence models (e.g. LES or DES) under yaw and slant variations are still rare. Meanwhile, experimental studies often lack the comprehensive pressure mapping or wake visualization under combined yaw and slant angle conditions, leading to incomplete understanding of flow dynamics. On the whole, while substantial research has been conducted on the aerodynamic drag reduction using passive and active techniques, the combined influence of yaw angle and slant angle on the aerodynamics of Ahmed body remains inadequately addressed. Furthermore, the interaction between passive devices like VGs and complex flow conditions involving yaw and slant angles is poorly understood. This study aims to address this gap by experimentally investigate the aerodynamic behavior of the Ahmed model under various yaw and slant angles, with and without the passive control devices. The objectives include evaluating the resultant pressure distribution and drag force alteration from the different configurations.

2. Methodology

Without changing the projected frontal area of the vehicle, it is still possible to modify its shape in a more streamlined way. External attachments can help minimize the aerodynamic drag based on their external shape, size and placement. Aerodynamic drag (D) depends on the size of a vehicle (projected frontal area, A), drag coefficient (C_D) that is a measure of the flow quality around the vehicle, and the square of the vehicle speed (V) as expressed as in Equation 1.

$$D = \frac{1}{2} C_D \rho V^2 A \tag{1}$$

Dynamic pressure (velocity pressure) is the increase in a moving fluid's pressure over its static value due to motion. In incompressible fluid dynamics, it is indicated as q and is defined in Equation 2, where q is the dynamic pressure in Pascal, ρ is the fluid density in kg/m^3 and V is the flow speed in m/s.

$$q = \frac{1}{2} \rho V^2 \tag{2}$$

Another important aspect of the dynamic pressure is that the aerodynamic stress (i.e. stress within a structure subject to aerodynamic forces) experienced by a vehicle travelling at speed V is proportional to air density and square of V (i.e. proportional to q). Hence, by looking at variation of q, it is possible to determine how the stress will vary and, in particular, when it will reach its maximum value. The point of the maximum aerodynamic load is often referred to as “maximum q” and it is a critical parameter in many applications such as launch vehicles.

Moreover, pressure coefficient (C_p) is the parameter for studying the flow of incompressible fluids such as water and also the low-speed flow of compressible fluids such as air. The relationship between this dimensionless coefficient and the dimensional numbers is given by Equation 3, where P is the static pressure at the point at which the pressure coefficient is being evaluated, Ps is the static pressure in the freestream (i.e. remote from any disturbance), ρ is the freestream fluid density (i.e. for air at the sea level and 15 °C is 1.225 kg/m³) and V is freestream velocity of the fluid, or the velocity of the body through the fluid.

$$C_P = \frac{P - P_S}{\frac{1}{2}\rho V^2} \tag{3}$$

The pressure coefficient describes the relative pressures throughout a flow field in fluid dynamics. It is used in aerodynamics and hydrodynamics, whereby every point in the fluid flow field has its own unique pressure coefficient. In many situations, the pressure coefficient at a point that is near a body is independent of body size. Consequently, an engineering model can be tested in a wind tunnel or water tunnel through which the pressure coefficients can be determined at critical locations around the model and these pressure coefficients can be used with confidence to predict the fluid pressure at those critical locations around a full-size vehicle.

For this study, an experimental study on an Ahmed model is conducted using the wind tunnel. The resulting data is collected and analyzed to test the resulting flow separation from different yawing angle with the slant back angle of 0°, 15°, 25° and 45°. The model has also been set at various angles of yaw of -25°, -20°, -15°, 0°, 25°, 20° and 15°. The model used for this project is an Ahmed model from the UTM Aero lab, which is a 1:16 scale replica constructed from high-strength, vibration-resistant wood. While the material's surface finish can influence the boundary layer behavior and also flow separation, the model’s surface is maintained with a smooth finish to reduce roughness effects in this study. This model is built for use in wind tunnel testing and has been made to place pressure vessels to be connected to the pressure scanner. This model has a weight of almost 2 kg and can withstand the wind speed and pressure when the test in the wind tunnel is carried out. Figure 1 shows the overall view of the applied generic Ahmad model in this study and Table 1 tabulates its main dimensions.

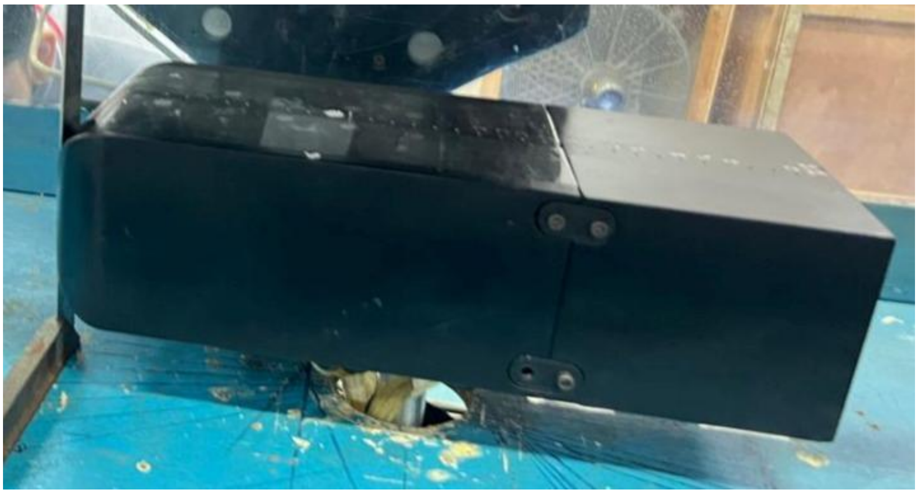

Figure 1: Generic Ahmed model used in the wind tunnel testing

Table 1: Dimensions of the Ahmed model

Part	Description	Dimension (mm)
A	Overall Length	350
B	Overall Width	120
C	Overall Height	130

The wind tunnel experiment is conducted at Universiti Teknologi Malaysia Aeronautics Laboratory (UTM Aerolab). The test section for putting the model is 2.0 m (width) x 1.5 m (height) x 5.8 m (length) and the wind tunnel is a closed-return low speed type. In this study, this model is tested on 3.2 x 10^6 and 3.7 x 10^6 Reynolds Numbers. This wind tunnel can generate airflow up to a Mach speed of 0.23 or 80 m/s in the test section area. It has the flow and temperature uniformity of less than 0.15% to 0.20%, respectively, and less turbulence from 0.06%. Figure 2 shows example of the Ahmed model used with different slant angles while Figure 3 depicts the pressure scanner used in the testing.

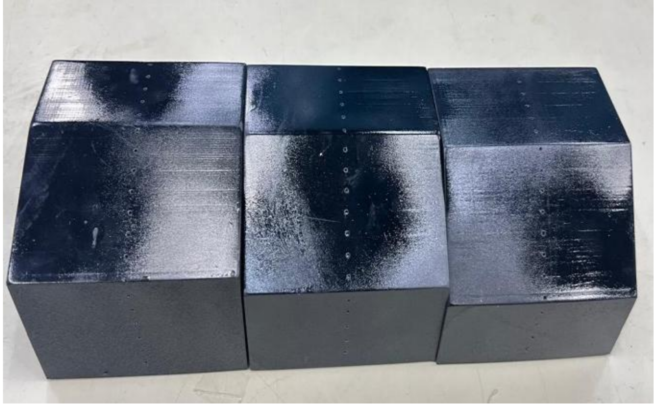

Figure 2: Ahmed Model slant angles of 15°, 25° and 45°

Figure 3: Pressure scanner used in this study

In short, the experiment is conducted in a subsonic wind tunnel and the wind speed has been set within a controlled range to analyze both pressure and force. The Ahmed model is mounted in the test section of the wind tunnel and a series of pressure sensors (approximately 2 mm in diameter) have been installed at specific locations on the model's surface to capture the pressure variations due to the vortex interactions. These sensors are connected via urethane tubing to a data acquisition system for real-time recording. Depiction of this wind tunnel setup can be seen in Figure 4. It should be noted that the usage of a closed-return low speed wind tunnel for this study allows for a spacious environment to minimize the wall effects and ensure uniform airflow across the model. All in all, the experimental matrix for this study consists of testing four different Ahmed models with slant back angles of 0°, 15°, 25° and 40° at seven settings of yaw angles of -25°, -20°, -15°, 0°, 15°, 20° and 25°. Note that the wind tunnel test for each configuration is repeated three times to ensure data repeatability, with the average value used for analysis. Error margins have been quantified through standard deviation calculations. Prior to each test, sensors and equipment are calibrated to minimize measurement uncertainties.

Firstly, the generic Ahmed model is properly mounted on the wind tunnel test section. Next, the pneumatic piping of the pressure scanner is mounted at the surface body of the model. In addition, the load cell is also mounted at the model's surface body. Once these have been securely mounted on the model, the wind tunnel test can be conducted. In this study, the test is conducted at seven different yaw angles of -25°, -20°, -15°, 0°, 25°, 20° and 15° while the wind speed in the tunnel during the testing has been set to 25 m/s. Once the test is completed, the model is changed with the next Ahmed model with a different slant back side angle and the wind tunnel test is conducted again. This is repeated until all of the four Ahmed models with the different slant back angle have been successfully tested. The collected experimental data is then analyzed to establish the effects of the different model configurations. In this case, effects on adverse pressure gradient and flow separation are observed using the pressure scanner while effects on force are observed using the load cell's digital sensor. Moreover, the flow visualization data is done through the pressure distribution method.

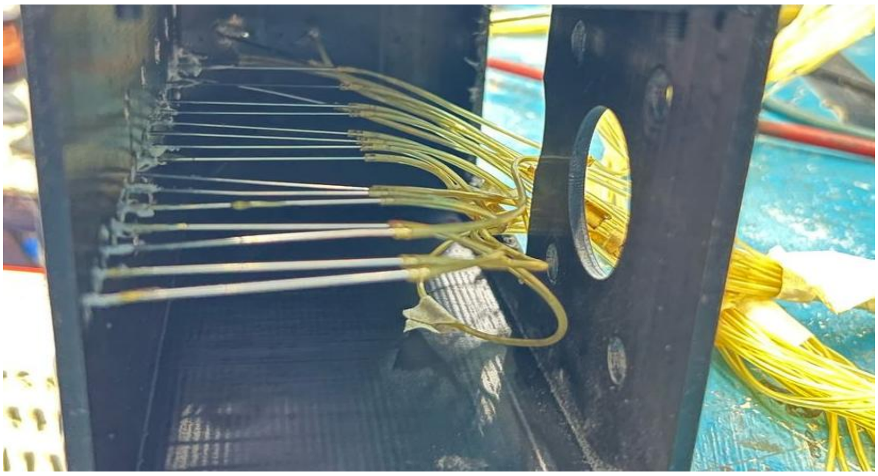

Figure 4: Pressure tap located at the model's top surface and back slant

It should be noted that all of the experimental procedures in the conduct of this study have been documented to allow replication. The model specifications, wind tunnel conditions and data processing techniques ensure that similar results can be achieved in future conduct of the similar procedures. This methodology provides a structured experimental approach to analyze aerodynamic behavior of Ahmed model's pressure and force with different yawing angles and slant back side angles.

3. Results and Discussion

The obtained experimental results are shown in Figure 5 to Figure 8, which provide the behaviors of impact pressure and aerodynamic drag force that can contribute towards a better understanding of the maneuvering of the Ahmed model. The experimental data can also be used to aid in the validation of simulation models. In automotive applications, the chosen yaw angles represent the typical vehicle maneuvering scenarios such as turning or side-slip conditions, which are critical for understanding flow separation and pressure distribution. The slant back angles have been selected to simulate different rear vehicle geometries that influence aerodynamic stability and drag. Moreover, Reynolds numbers of 3.2×10^6 and 3.7×10^6 have been targeted to emulate the realistic driving conditions under turbulent flow regimes, consistent with standard operating speeds for vehicles. These parameters collectively facilitate a comprehensive analysis of the model's aerodynamic performance across practical scenarios.

On the whole, the results from this wind tunnel testing of the UTM Generic Ahmed Model reveal that yaw angle plays a dominant role in influencing the aerodynamic behavior of the model. Specifically, changes in the yaw angle lead to significant variations in the pressure coefficient (C_p) and aerodynamic drag coefficient (C_D) across top and rear surfaces of the model. As the yaw angle increases, the pressure distribution becomes increasingly asymmetric, which directly correlates with the changes in the flow separation and wake formation. In addition, it has been also observed that the position of the pressure taps, particularly on the top and rear surfaces, is crucial for capturing accurate variations in the pressure. These areas exhibit the highest sensitivity to changes in yaw angle and can provide a clear representation of how surface pressures are redistributed under non-zero yaw conditions. In contrast, the Reynolds number is shown to have minimal influence on both pressure and force coefficients within the tested flow velocity range. This suggests that the aerodynamic performance of the Ahmed model is primarily governed by yaw angle effects rather than changes in the speed of the flow.

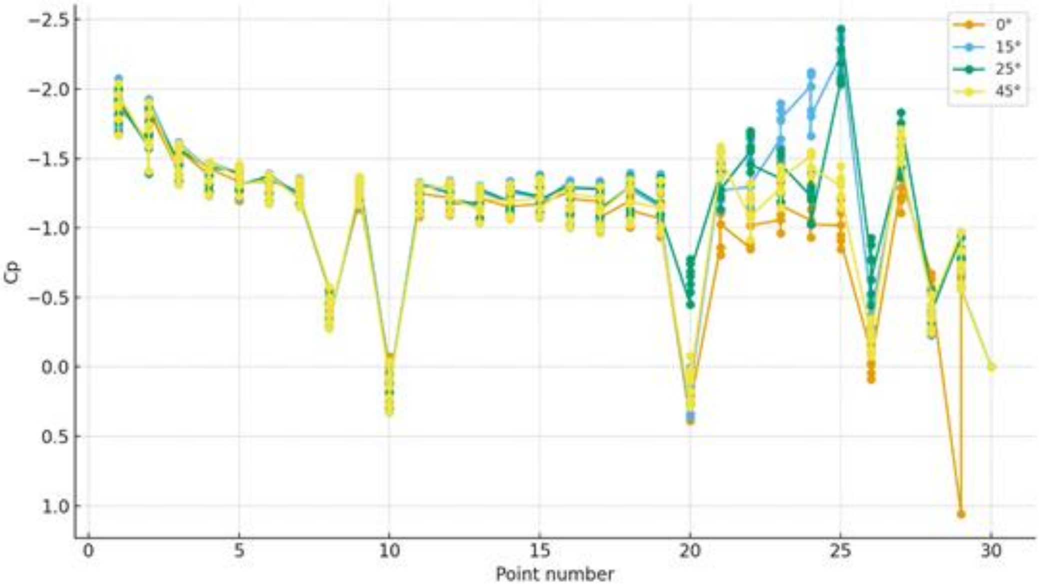

Figure 5: Pressure coefficient distribution over Ahmed model in different back slant angles at yaw angle of -25° and velocity of 25 m/s

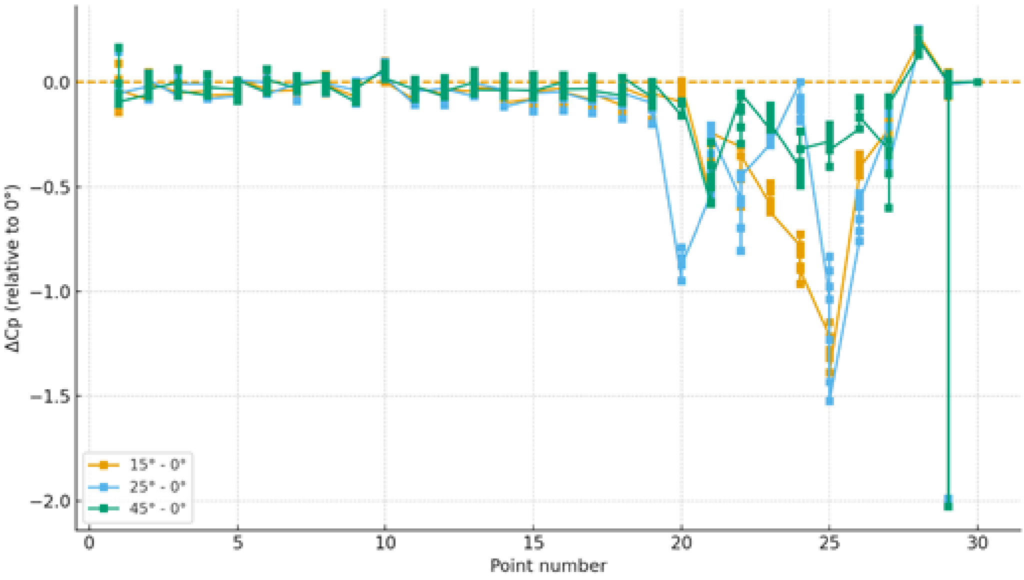

Figure 6: C_p value due to slant angle negative (stronger suction)

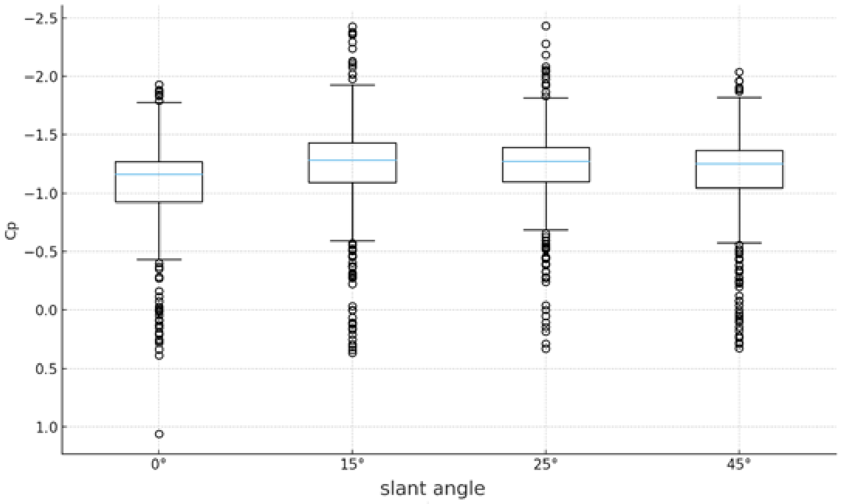

Figure 7: Distribution of C_p by slant angles

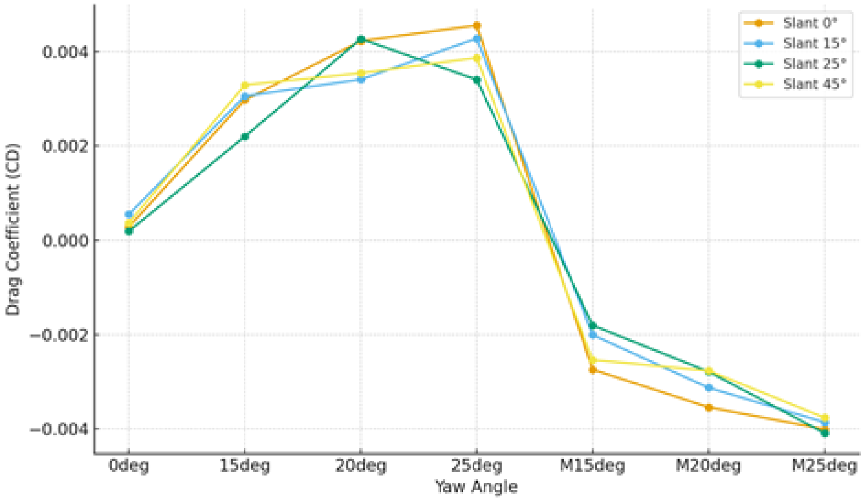

Figure 8: C_D at different yaw and slant back angles

While the experimental setup in this study has provided a valuable insight into the impact of yaw angle on flow behavior, several limitations are also acknowledged as listed below:

- The tests were conducted in a low-speed wind tunnel, restricting the range of Reynolds numbers and limiting comparison to full-scale vehicle conditions.
- Pressure measurements were obtained only from the top and rear surfaces of the model. The flow features on the side surfaces and underbody, which are also affected by the yaw angle, were not captured.
- The study was based on a simplified Ahmed body and did not include real-world features such as rotating wheels, undertray effects or ground clearance variations.
- No flow visualization or turbulence measurements via smoke, tuft grids or PIV were performed, which limits interpretation of three-dimensional flow behavior.

4. Conclusion

This study is aimed to experimentally investigate the aerodynamic behavior of the Ahmed model under various yaw and slant angles, with and without the passive control devices. The focus of the study is on the pressure distribution and drag force alteration from the different configurations. Based on the results of the conducted wind tunnel testing of the Ahmed Model, it has been demonstrated that yaw angle has a dominant role in influencing the aerodynamic behavior of the vehicle model. Specifically, changes in the yaw angle lead to significant variations in the pressure coefficient (C_p) and aerodynamic force coefficients (C_D). As yaw angle increases, pressure distribution becomes increasingly asymmetric, which directly correlates with the changes in flow separation and also wake formation. To build upon the findings of this research, the following future directions are recommended:

- Expand the Reynolds number range to include higher-speed conditions and evaluate scale effects more comprehensively.
- Incorporate side and underbody pressure taps, or utilize advanced measurement techniques such as Particle Image Velocimetry (PIV) or Laser Doppler Anemometry (LDA), to visualize complex flow structures and quantify turbulence characteristics.
- Introduce active and passive flow control devices, such as vortex generators, Coanda-effect nozzles, or synthetic jets, to assess their effectiveness in mitigating yaw-induced aerodynamic penalties.
- Investigate the effects of rotating wheels, ground proximity (ride height), and underbody flow, which play a crucial role in real vehicle aerodynamics.
- Combine CFD simulations with experimental data to develop a more comprehensive understanding of the aerodynamic phenomena and validate computational models under yaw conditions.

Acknowledgement

The authors would like to acknowledge that this study is funded by Universiti Teknologi Malaysia through their research grant scheme (Grant No. 22H81). In addition, special acknowledgement to the technical staff of Aerolab UTM (Universiti Teknologi Malaysia) for the use of their assistance.

References

[1] S. R. Ahmed, G. Ramm and G. Faltin, “Some Salient Features of the Time-Averaged Ground Vehicle Wake,” SAE Transactions, vol. 93, pp. 473–503, 1984.

[2] N. A. Siddiqui and M. A. Chaab, “A Simple Passive Device for the Drag Reduction of an Ahmed Body,” Journal of Applied Fluid Mechanics, vol. 14, no. 1, pp. 147-164, 2020.

[3] B. Harinaldi, R. Tarakka and S. P. Simanungkalit, “Computational Analysis of Active Flow Control to Reduce Aerodynamics Drag On A Van Model,” International Journal of Mechanical & Mechatronics Engineering, vol.11, no. 3, pp. 24-30, 2011.

[4] C. Bayındırlı and M. Çelik, “Drag Reduction of Ground Vehicle by Decreasing Flow Separation With A Passive Flow Control Part,” Uluslararası Mühendislik Tasarım ve Teknoloji Dergisi, vol. 6, no. 2, pp. 96-102, 2024.

[5] H. Viswanathan, “Aerodynamic Performance of Several Passive Vortex Generator Configurations on an Ahmed Body Subjected to Yaw Angles,” Journal of the Brazilian Society of Mechanical Sciences and Engineering, vol. 43, no. 3, 131, 2021.

[6] C. García-Baena, J. M. Camacho-Sánchez, M. Lorite-Díez, C. Gutiérrez-Montes and J. I. Jiménez-González, “Drag Reduction on a Blunt Body by Self-Adaption of Rear Flexibly Hinged Flaps,” Journal of Fluids and Structures, vol. 118, 103854, 2023.

[7] A. Şumnu and Yüksel Eraslan, “Aerodynamic Shape Optimization of Simplified Ground Vehicle (Ahmed Body) using Passive Control Devices,” Mechanics, vol. 31, no. 1, pp. 5-14, 2025.

eISSN 3009-0520
9 773009 052004